

High Accuracy Protein Identification: Fusion of solid-state nanopore sensing and machine learning

Shankar Dutt^{1, γ, *}, Hancheng Shao^{1, γ}, Buddini Karawdeniya², Y. M. Nuwan D. Y. Bandara³,
Eleni Daskalaki⁴, Hanna Suominen⁴, Patrick Kluth¹

¹Department of Materials Physics, Research School of Physics, Australian National University, Canberra ACT 2601, Australia

²Department of Electronic Materials Engineering, Research School of Physics, Australian National University, Canberra ACT 2601, Australia

³Research School of Chemistry, Australian National University, Canberra ACT 2601, Australia

⁴School of Computing, College of Engineering and Computer Science, Australian National University, Canberra ACT 2601, Australia

γ: These authors contributed equally.

*Email: shankar.dutt@anu.edu.au

ABSTRACT

Proteins are arguably the most important class of biomarkers for health diagnostic purposes. Label-free solid-state nanopore sensing is a versatile technique for sensing and analysing biomolecules such as proteins at single-molecule level. While molecular-level information on size, shape, and charge of proteins can be assessed by nanopores, the identification of proteins with comparable sizes remains a challenge. Here, we present methods that combine machine learning (ML) with nanopore sensing to address this challenge. We assess the translocations of the proteins using amplifiers with bandwidths (BWs) of 100 kHz (sampling rate=200 ksps) and 10 MHz (sampling rate=40 Msps), the highest bandwidth reported for protein sensing, using nanopores fabricated in <10 nm thick silicon nitride membranes. Identification accuracies of up to 66% and 83% (without clustering) were achieved with 100 kHz and 10 MHz BW instruments, respectively. The accuracy of protein identification was further enhanced by grouping the signals into several clusters depending on the event features with identification accuracies of up to 89% for combinations of four proteins. The combined improvement in sensor signals through use of high bandwidth instruments combined with data analysis methods, clustering and machine learning, allows identification of proteins with high accuracy.

1. INTRODUCTION

Proteins are arguably the most important class of molecules in biological processes with diverse functionalities. They can serve as biomarkers for diagnosis and monitoring of diseases, facilitate cellular signaling and reaction catalysis, and enable transport and storage of critical ions and molecules¹⁻⁶. Proteins are constructed of amino acid chains folded into specific tertiary and quaternary structures that govern their function. While proteins are vital actors for biological processes and functions essential for life, their presence or fluctuations of their typical levels can also indicate detrimental biological processes (and their stage) such as adverse health conditions. In some circumstances, proteins contribute to the advancement of diseases by intensifying their activity to create favorable settings that enhance the progression of the disease, e.g. proteins such as PADI4 and HIF-1 facilitate the growth of cancer⁷⁻⁹. Irrespective of the function, selective protein detection and quantification is critical for the identification, evaluation and understanding of biological processes and related progress, e.g., for future drug development.

Complex biological samples like serum, saliva, or urine contain a multitude of protein biomarkers indicative of a host of health conditions. There are numerous conventional analytical methods for protein detection, characterization, and quantification such as mass spectrometry (MS)^{10,11}, protein NMR spectroscopy¹², enzyme-linked immunosorbent assay (ELISA)¹³, protein immunoprecipitation¹⁴, X-ray crystallography¹⁵ and fluorescence resonance energy transfer (FRET)¹⁶. While these have seen widespread adoption as tools for protein profiling, inherent challenges include tedious sample preparation and complex instrumentation (MS), protein labeling (FRET), the need for specific receptors (ELISA), biologically active crystalline states (X-ray), and advanced expertise in using these techniques. A label-free,

portable technology with minimal sample preparation, with the ability to operate in biomimetic fluids for selective detection of low-abundance targets (i.e., for early detection) in complex samples could be transformative (i.e., many tests in one platform). While lateral-flow-assay-based point-of-care devices tick most of these boxes, they are designed for the visual detection of a specific target using specific receptors and may not be ideal for the early detection of a health condition (i.e., low abundance assaying).

In this study, we use a solid-state nanopore (nanopore hereafter) sensor and machine learning (ML) for the selective identification of four similar-sized proteins. A nanopore sensor, in its simplest definition, is a nanoscale aperture spanning an otherwise impervious membrane separating two electrolyte reservoirs. The analyte is added to one side (*cis* side) and a suitable voltage is applied to the other side (*trans* side) to drive the molecules across the nanopore generating analyte-specific information as resistive or conductive pulses. Importantly, nanopore sensing can be conducted under various electrolyte chemistries and the sample is typically added as-is. The versatility of this tag-free technology is well demonstrated by its application repertoire spanning a host of biological classes such as DNA^{17,18}, proteins^{19,20}, glycans^{21,22}, viruses^{23,24}, and liposomes²⁵. Unsurprisingly, nanopores have also demonstrated great potential in studying the fundamental protein structure as well as its biochemistry and biophysics. For example, protein flexibility²⁶, folding-unfolding²⁷, molecular weight²⁸, conformational differences²⁹, and interaction with proteins³⁰ have been studied using nanopores. A key challenge in protein sensing is the fast translocation speed associated with proteins. With a conventional Axopatch 200B amplifier in the resistive-feedback mode, translocations with residence times less than 10 μ s are attenuated²⁸. Thus, there is a constant interest to perform nanopore sensing experiments using MHz-level bandwidth (BW) equipment as they allow sub-microsecond resolution readouts. The caveat with higher bandwidth is the increasing open-pore current noise which can be circumvented partially by

noise reduction (e.g., membranes fabricated employing low dielectric noise materials such as quartz³¹) and signal magnitude enhancement (e.g., thinner membranes) strategies. For nanopore-based protein sensing experiments, the highest bandwidth reported to date is 1 MHz³², and for DNA bandwidth up to 10 MHz^{31,33} has been reported. In this study, we report the detection of proteins with bandwidths up to 10 MHz (sampling rate of 40 Msps). The high bandwidth is instrumental for the distinction between four similar sized proteins using machine learning.

One of the main challenges of nanopore sensing has been the selective identification of analytes in a complex mixture by electrical readouts alone. That is, uniquely associating the resistive/conductive pulse of the nanopore sensor to a specific analyte. While modifying the nanopore surface with a selective receptor such as an antibody or an aptamer could incorporate the much-needed selectivity, the shelf-life of the functional layers, device-to-device variability, sensitivity/susceptibility to electrolyte conditions, biofouling (in the case of complex-samples) and limited throughput could cripple the anticipated selectivity. The lack of selectivity is exacerbated by the fact, despite being a single molecule sensor, the individual waveforms resulting from translocations have so far been mainly characterized by two parameters: the pulse width (i.e., translocation time; Δt) and pulse depth (ΔI). In certain instances, the area of the event, noise levels and stepwise information of events were also used for analysis which are correlated to the pulse width and pulse depth^{34,35}. While these parameters can generate a fingerprint of a molecule leading to identification, for molecules of very similar weight, size, and charge in a complex mixture, accurate identification with such simple metrics alone is hardly possible. This type of conventional analysis leads to an enormous loss of data since each waveform is just characterized by two features (i.e., Δt and ΔI). Using an increasing number of features of the signal or even the entire signal renders conventional statistical analysis extremely difficult which is further exasperated by the number of different signals that can

result from one analyte. Thus, supervised ML approaches become attractive for analyte identification. The use of such ML approaches has gained tremendous traction in DNA sequencing³⁶, and the determination of structural composition of polysaccharides³⁷. Additionally, identification of larger particles such as bacteria and viruses are also emerging triggered by the current pandemic and other global disease outbreaks. This is exemplified by the works of Tsutsui *et al.*³⁸ (bacteria) and, Taniguchi *et al.*²³ (virus) where solid state nanopores and machine learning methods were combined to discriminate between single-bacterial shapes and to identify coronaviruses, respectively. For proteins, Raynaud *et al.*³⁹ used seven features to distinguish a binary protein mixture, currently the only existing machine learning-incorporated protein sensing study using functionalized nanopores. Here we present a quaternary protein system with data acquisition in the challenging 10 MHz domain (compared to the conventional 100 kHz) and >29,000 events on average (for different proteins measured at different applied bias) ($\sim 76 \times$ higher the previously mentioned study). Nanopore data undoubtably deliver sufficient information to differentiate proteins (biomolecules in general), yet as evident by the literature, classical analysis techniques are not deciphering the additional layers of information encoded in nanopore waveforms. In this study, we explore ML coupled with solid-state nanopores for identification and discrimination of proteins to elevate the potential of this already powerful single-molecule sensing tool for protein sensing.

2. RESULTS

2.1 Fusion of nanopore sensing and machine learning

Figure 1(a) shows a schematic of protein translocation through a ~ 7 nm thick silicon nitride membrane. The translocation measurements were done using two portable amplifiers developed by Elements srl (Figure 1 (b)) with bandwidths of 100 kHz (200 ksps) and 10 MHz

(40 Msps). In this investigation, we considered four proteins (Hb, HSA, BSA, and Con A) because of their similar molecular weights and/or sizes (Table S1). Proteins with significantly different sizes and/or molecular weights will generate (very) distinct electrical readouts and are thus (relatively) easy to distinguish. The choice of proteins was therefore made to imitate a challenge that arises when trying to identify similar-sized proteins in complex real-world solutions, such as blood serum. Representative current-time traces from translocation measurements at 200 ksps (BW=100 kHz) and 40 Msps (BW=10 MHz) are shown in Figure 1(d) and (e) respectively. Figure 1 (f) and (g) illustrate an example of unfiltered signals produced by measurements at 200 ksps and 40 Msps, respectively followed by lowpass filtering with various cut-off frequencies. As expected, reducing the cut-off frequency reduces the overall noise of the measurement yet with loss of signal characteristics that are essential for machine learning-based categorisation. The intricacies of the signal structure are almost completely lost with ubiquitous 10 kHz cut-off frequency emphasizing the need for higher bandwidth instrumentation for nanopore sensing^{20,40,41}. While this frequency has its merits for conventional two-metric analysis based on Δt and ΔI , the loss of intricate intra-signal details makes it inefficient for current study. For measurements made at 200 ksps and 40 Msps, we thus chose cut-off frequencies of 35 kHz and 100 kHz, respectively, because these frequencies had the greatest signal-to-noise ratios while still maintaining the fine features of the signals.

Under an applied bias of 500 mV, the histograms for relative changes in conductance ($\Delta G/G$), dwell time (Δt), and scatter plots exhibiting $\Delta G/G$ as a function of Δt are shown in Figures 2(a) and (e) for all proteins. Other voltage-specific histograms and scatter plots are provided in the SI (figures S1, S2, S4, S5). As can be observed through scatter plots, the collected signal with different bandwidths under otherwise similar conditions show distribution of dwell times noticeably different from each other. This is expected considering that the Elements 10 MHz

amplifier can operate at a $100\times$ higher bandwidth compared to the Elements 100 kHz amplifier. For ease of comparison, histograms corresponding to $\Delta G/G$ for the four proteins investigated with the 100 kHz instrument (200 ksps, BW=100 kHz, LPF=10 kHz) and the 10 MHz instrument (40 Msps, BW=10MHz, LPF=100 kHz) are shown in Figures 2(b)-(d) and (f)-(h). We observe significant overlap of the histograms because the protein sizes or molecular weights are similar. A closer look reveals that the histograms change with applied bias, and for certain data, two distributions are visible, which indicates different preferred protein conformations under different applied voltages. Figures S3 and S6 depict the overlapping histograms corresponding to the change in dwell duration for different applied biases, further supporting the usage of machine learning for this challenge.

Machine learning was performed to identify the proteins using the methods described in Methods section (Figure 3a). The quality of the input(s) to the algorithm determines how well the classifier performs. Five distinct feature extraction algorithms were created for each of the schemes (figure 3b, table 1) to extract the features in segmented and whole waveforms needed for machine learning. The confusion matrices produced by the machine learning classification corresponding to the four proteins by measurements taken at 200 ksps and 40 Msps in response to 500 mV are shown in Figure 3(c) and (d). Figure 3 (e) and (f) demonstrate the corresponding identification accuracy for dual, tri and quaternary protein systems. For this data, feature extraction scheme 3 (see table 1) was applied. The fine features of waveforms are more apparent with the 10 MHz amplifier compared to its 100 kHz counterpart due to significant bandwidth difference and the ability of the former to sample data at 40 Msps while the latter is only capable of sampling at 200 ksps: a 50 μ s long event would be portrayed by 2000 points with the 10 MHz amplifier while with the latter it would be limited to 10 data points. These differences are well reflected in the F-value where identification accuracy obtained with at 10

MHz bandwidth instrument was 0.79, as opposed to 0.66 with 100 kHz bandwidth instrument. The impact of measurements under different bias on the identification accuracies is discussed below.

2.2 Effect of Clustering on Identification Accuracies

As proteins are complex charged molecules (with both charged and hydrophobic moieties), they often show physiochemical interactions with the nanopore membranes¹³. These interactions (both specific and non-specific) include, for example, the adsorption to the nanopore surface and, protein-protein interactions. Such interactions can be protein specific or can be inherent to the nanopore system. We divided the waveforms into various individual clusters based on the features of the waveform which may be an indication of the smooth translocations and different interactions as discussed earlier. These are shown in Figure 4(a) and (b), which correspond to measurements done at 200 ksps and 40 Msps, respectively. The clusters shown correspond to data measured under a bias of 500 mV. Clusters for the other applied biases are given in Figures S7 - S10. In addition to the cluster centres, the distinct waveforms are also displayed using thin lines with a transparency of 80%. Cluster 0 with the highest population was associated with smooth translocations of the proteins. Although it is difficult to determine which sort of interactions lead to a particular cluster based on this data, proteins moving closer to the pore surface (more pore-surface interactions and by extension higher confinement) would have longer dwell times compared to the translocations along the principal axis (i.e., smooth translocations). For certain clusters, we also see a brief rising time followed by a prolonged crest, which is another sign of a transient change brought on by the physical confinement of the biomolecule or induced by the electric field of the nanopore. We extracted features from the waveforms associated with specific clusters using Scheme 3 and utilised those features to train and test the data in order to investigate the impact of generated clusters on the

identification of proteins. Figure 4(c) shows the identification accuracies for the case of four proteins as a function of waveforms belonging to different clusters. The blue and red hues represent the F-values from measurements done at 200 ksps and 40 Msps, respectively. It is apparent that cluster 0 has the lowest F-value that we believe to be from smooth translocations. The waveforms belonging to cluster 1-3 are believed to be the result of different protein-pore interactions and have much higher F-values. In particular, clusters 1 and 2 show F-values of 0.75 and 0.73, respectively, for measurements done at 200 ksps. For measurements carried out at 40 Msps, the F-values increased to 0.85 (cluster 1) and 0.89 (cluster 2), demonstrating that the various proteins interact with the nanopore system in very different ways and that the signals or waveforms produced by these interactions enable more precise discrimination between these four proteins.

2.3 Effect of Feature Extraction scheme on Identification Accuracies

As was previously mentioned, accuracy of the classifiers depends on the goodness of the data fed into the process. As a result, we evaluated the accuracy values for the identification of the quaternary-protein system using various feature extraction techniques. The F-values (corresponding to the combination of four proteins) are displayed in Figure 4(d) as a function of the various schemes. Scheme 3 provided the highest accuracy for measurements done at both 200 ksps and 40 Msps. As compared to Scheme 1, we saw a significant increase in the F-values obtained from Scheme 3 showing the importance of using a multi-feature approach and the significance of features such as area under the curve, the tailedness and the asymmetry of the waveform. Scheme 4 was not used with the data resulting from measurements done at 200 ksps as at this sampling rate as the waveform does not have enough data points to enable the division of the waveform into 50 parts. Despite being highly computationally costly, Scheme 5, which uses the entire signal as an input along with some characteristics about the waveform

shape, did not show increased F-values as compared to Scheme 3 and was thus not employed for the data obtained from measurements carried out at 40 Msps.

2.4 Effect of LPF on Identification Accuracies

Figure 4 (e) shows the impact of different cut-off frequencies of the LPF on the F-values. A 10 kHz LPF is often used for filtering raw data to increase the SNR with some studies using 5 kHz cut-off frequencies^{18,42}. However, as shown in Figure 1(f), at these cut-off frequencies (i.e., 5 kHz and 10 kHz), essential information in the signals is lost. The accuracy of the results produced by the classifier is directly impacted by the loss of information as a result of choosing low cut-off frequencies. On the other hand, noise in the waveform can also reduce the accuracy if the signal is not adequately filtered. The values shown in Figure 4(e) clearly demonstrate this where an optimal cut-off frequency is needed to maximize the F-values. When measurements were conducted at 200 ksps, the signals filtered at 35 kHz produced better F-values, while measurements conducted at 40 Msps produced the best results when filtered at 100 kHz. At higher cut-off frequencies (500 kHz), the data was noisier and the SNR was poor. Although lower frequency (35 kHz) filtering improved the SNR of the waveform, it comes at the expense of finer information within the waveform. For measurements taken at 200 ksps and 40 Msps, the data was thus filtered at 35 kHz and 100 kHz, respectively, and was used to produce all other results described in this study.

2.5 Effect of Applied Bias on Identification Accuracies

We also investigated how the applied voltage during the measurements affected the accuracy of protein identification. The applied voltage has been shown to influence the translocating conformation of proteins. Furthermore, the applied voltage and residence time are inversely correlated (with few exceptions such as in instances where voltage-mediated protein unfolding

is taking place). To study the effect of voltage on the identification accuracy, we computed the F-values resulting from measurements performed under different applied biases (i.e., 300mV, 400mV and 500mV). For both the measurements done at 200 ksps and 40 Msps, the lowest F-values were obtained for experiments under 400 mV. The highest F-values obtained for 200 ksps and were 40 Msps data were 0.66 (500 mV) and 0.83 (300 mV), respectively. While one would generally expect to see a higher F-value at lower voltages due to slow translocation speeds, it is interesting to note the lack of any linear correlation with the applied voltage and the F-value in the two cases. Since proteins are sensitive to the voltage bias used for translocation experiments unlike more rigid structures like DNA, this result further emphasizes the need to probe the translocations over multiple voltages rather than choosing an arbitrary voltage bias.

3. DISCUSSION

Machine learning is highly promising for the identification of similar-sized proteins with high accuracy using single molecule nanopore measurements. Since the measurement platform makes use of solid state nanopores, there is a small tolerance for variation in the diameters of the nanopores between membranes. We were able to translate the trained data from one nanopore and test it with a brand-new set of data from another nanopore and obtained almost identical accuracies (within 3%) owing to the standardisation procedures (using the open pore conductance to normalise the conductance drop) utilised in the current work. The portable 10 MHz bandwidth amplifier yields detailed signals that improve identification accuracy significantly compared to commonly used 100 kHz amplifiers. We demonstrated that the identification accuracy varies with the applied trans-membrane bias which could be associated to the presence of different protein conformations at different voltages. With accuracies as high as 99.3%, we observed extraordinarily strong discrimination between proteins of comparable

sizes in two protein combinations. With the help of clustering and high bandwidth measurements, accuracies as high as 89% are obtained for combinations of four proteins. The fusion of solid state nanopore sensing and machine learning is thus very promising for the identification of proteins in complex samples. Selectivity has been a major challenge in label free nanopore sensing and this is an important step towards addressing this challenge. For our study, widely used thin SiN_x membranes were employed. Methodologies to slowdown the translocation of the proteins through solid state nanopores and reduce dielectric noise can yield further improvements in data quality that can further increase accuracy. Our methodology offers the possibility to study variations in post-translational modifications of proteins, and protein-protein interactions that may also provide important insights into the underlying processes of diseases. Further enhancements, such as altering the kind of electrolyte, electrolyte concentration, and employing asymmetric electrolyte concentration in the cis and trans chambers, may be made to further increase our method's capacity to generate more confident identifications of the proteins, ushering in a new age in protein identification in complex solutions.

4. METHODS

4.1 Nanopore fabrication: Free standing, ~7 nm thick silicon nitride membranes with a ~100 nm thick silicon dioxide underlayer of size 40 mm x 40 mm on a 300 mm thick silicon frame were fabricated as discussed previously⁴³. The membranes were placed between two custom built PMMA half cells, with reservoirs containing a 1M KCl electrolyte solution buffered to a pH of ~7. A Keithely 2450 sourcemeter was used to apply an electric field <1 V/nm across the membrane, which was stopped as soon as a rapid surge in current was observed, indicating the creation of a nanopore^{44,45}. To estimate the size of fabricated nanopore,

a current-voltage (I-V) curve was obtained using the eNPR-200 amplifier: the slope of the curve (i.e., open-pore conductance, G) was then used to estimate the diameter of the pore using,

$$G_0 = K \left(\frac{1}{\frac{\pi r_0^2}{L_0} + \frac{\mu |\sigma|}{K} \frac{2\pi r_0}{L_0}} + \frac{2}{\alpha 2r_0 + \beta \frac{\mu |\sigma|}{K}} \right)^{-1}$$

Where L and d are membrane thickness and pore diameter, respectively. The diameter of the nanopores used in this investigation ranges from ~15 to 17 nm (cf. table S2).

4.2 Analytes and Data Acquisition: Information about the proteins (Bovine Hemoglobin (Hb), Human Serum Albumin (HSA), Bovine Serum Albumin (BSA), and Concanavalin A (Con A)) used in this study is given in table S1. Figure 1(c) shows the structure of the proteins obtained from the Protein Data Bank website of the Research Collaboratory for Structural Bioinformatics. 1M KCl (Sigma Aldrich, P9333) buffered with 10 mM tris-EDTA were used for all translocation experiments. The target protein was added to the *cis* side to a final concentration of ~23 nM. Using concentrated drops of HCl (Ajax-Finechem, AJA1367, 36%) or KOH (Chem Supply, PA161), the pH of the electrolyte was adjusted to the desired level and measured using an Orion StarTM pH meter. Figure 1(a) shows the schematic of protein translocation through a nanopore in response to a voltage bias applied to the *trans* side. We used two different portable amplifiers (Figure 1(c)): Elements nanopore readers with maximum bandwidths of a) 100 kHz and b) 10 MHz providing sampling rates of 200 ksps and 40 Msps respectively (these would hereafter be referred to as 100 kHz and 10 MHz amplifiers, respectively). While the 100 kHz amplifier produces data at bandwidths similar to conventional amplifiers such as Axopatch 200B used for the majority of nanopore experiments, the 10 MHz amplifier offers the highest-bandwidth measurements (giving a temporal resolution of 25 nanoseconds, generating data at a maximum rate of ~8.8 GB/min), enhancing the resolution of the electrical readouts³¹. As prolate shaped proteins are known to have preferred orientations

at different electric fields²⁹, the measurements were performed at voltages ranging from 300 mV to 600 mV (500 mV for measurements done at 10 MHz BW).

4.3 Lowpass filtration and waveform extraction: The acquired data was filtered using a 35 kHz and 100 kHz Butterworth filter for measurements done at 100 kHz BW (200 kbps) and 10 MHz BW (40 Msps), respectively. It was discovered that these cut-off frequencies offered the best signal-to-noise ratio without sacrificing details in the signal (see Results and Discussion section). The event extraction was done using a custom python-based code using vectorized operations from *numpy* and *bottleneck* libraries (see SI for the code and manual). An adaptive threshold (at or above $5 \times I_{\text{std}}$ where I_{std} is the standard deviation of the baseline in the analysis window) was used to flag the pulses to be extracted and stored (i.e., events or waveforms).

4.4 Clustering and feature extraction: The classification of the extracted waveforms into different clusters (based on similarity threshold of >85% determined by Pearson correlation) was done using a K-means algorithm⁴⁶. Each waveform is first assigned to a cluster at random by the K-means algorithm, which then repeatedly improves the clusters by shifting the waveforms to the cluster whose cluster centre is the most alike the waveform. The cluster centre shifts with each assignment, and the procedure is continued until either the cluster assignments cease shifting or a certain number of iterations has been reached. Four clusters were found to be the optimal number necessary for each cluster centre to offer details about various biomolecule translocation conformations through the nanopore without being too similar to other clusters (cf. Figure 4 (a, b)).

To employ both clustered and non-clustered waveforms for supervised learning, waveform characteristics other than conventionally used ΔI and Δt need to be extracted. These features

will be passed on to the classifier as input. As the shape, size, and surface charge of biomolecules vary not only from one species to another but also within the same species, the extraction of distinguishing features has a significant impact on the accuracy of the results. Figure 3(b) shows a schematic of several resistive pulse feature parameters. In brevity, the resistive pulse is divided into ‘n’ identical segments along its width where current drop at the median of each segmented signal ($\Delta i_1, \Delta i_2, \dots \Delta i_n$), pulse width at full width half maximum (t_{fwhm}), pulse width of each segment (t_0/n), drop in current at full width half maximum (i_{fwhm}), the maximum current drop (i_{max}), area under the curve, kurtosis (measure of asymmetry of the waveform) and, skewness (measure of the tailedness of the waveform), are used as key features for machine learning. All or some of these features were used for machine learning and the collection of the features used for the machine learning will hereafter be referred to as a scheme (see Table 1 for more details) We used five different schemes as shown in Table 1 and compared the accuracy of the results obtained from each (discussed in the Results Section).

4.5 Machine learning: We implemented supervised machine learning using random forest⁴⁷ and rotation forest⁴⁸ classifiers, supported by the large number of input waveforms (cf. table S3), and these classifiers adopt bagging or bootstrap sampling and scale well with high numbers of uncorrelated trees. Additionally, prior machine learning investigations involving the detection of viruses using solid-state nanopores have produced promising results using similar approaches^{23,24,49}. For the identification of the proteins considered in this investigation, we found that the random forest classifier performs slightly better than rotation forest (with F-values up to 6% higher with the random forest classifier). Thus, results corresponding to the random forest implementations are shown and discussed in this work hereafter. The classifier categorizes the results into four types: true positive, true negative, false positive and false negative and the ratio of these values gives the precision, recall and F-value (also referred to

as identification accuracies in this study). For training the algorithm, the data features from different proteins were binarized. The testing sets include a random combination of the data from different experiments of translocation of various proteins through different nanopores. Under-sampling was utilised to balance out the unequal datasets since the number of retrieved waveforms varies between measurements. This was done by maintaining all data in the minority class and reducing the size of the majority class. Random selection was used to choose the waveforms from the majority class. The models were implemented in Scikit-learn⁵⁰. An m-fold cross validation method ($m = 10$) was employed. As a result, each domain's data was first divided into training data and test data. The training data was then divided into 10 separate subsets at random. Each subset is used as a validation set once while other nine subsets are used as training set. The best model from the 10 training attempts is used as final model which is then evaluated on the initial test data. The final F-score shown in the study is obtained as an average over all regressions. For implementing machine learning on data resulting from different clusters, the raw waveforms originating from each protein (before the clustering procedure) were randomly divided into two parts with 80:20 split corresponding to raw training data (80%) and test data (20%). At this point, the data was split into various sets in order to remove any bias brought on by clustering and to prevent false high accuracy scores. Clustering was then carried out individually for each protein and each split. Then, depending on whether smooth translocations, interactions, or a combination of both should be the focus of the machine learning, waveforms from a certain cluster were chosen, and characteristics were then extracted from those waveforms. Following the under-sampling procedure, the data from several measurements were pooled. The test set was also treated in a similar fashion and the machine learning process was implemented as discussed earlier.

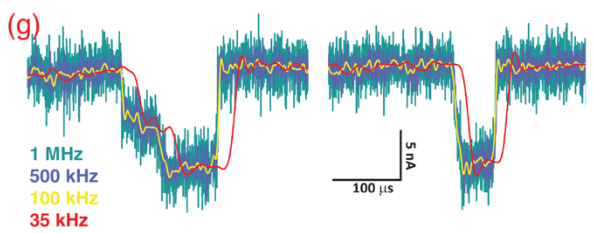
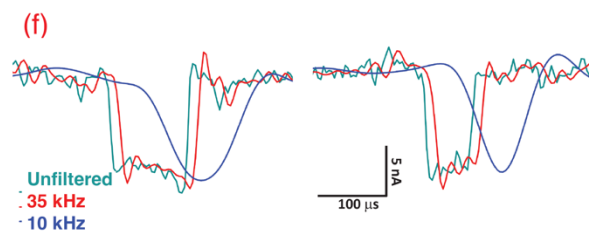
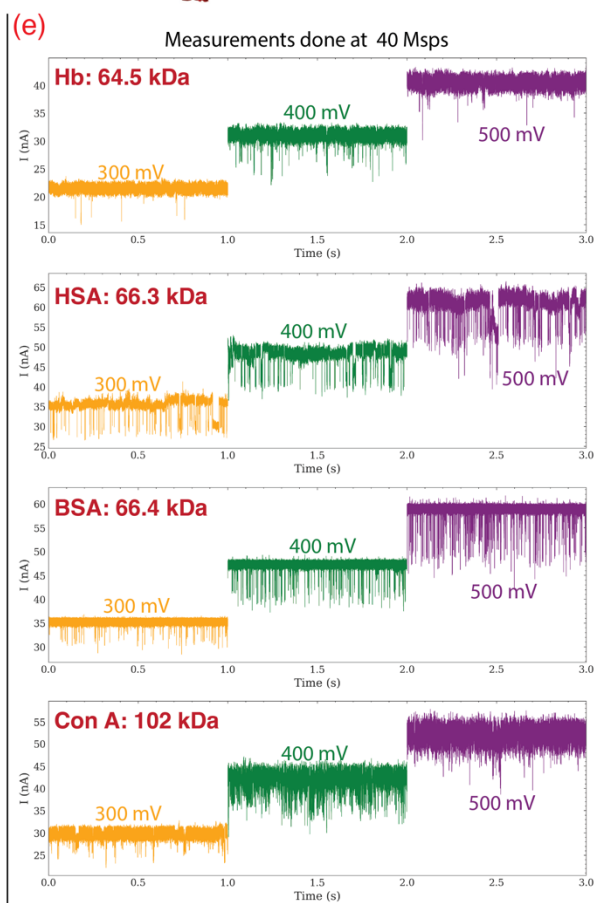
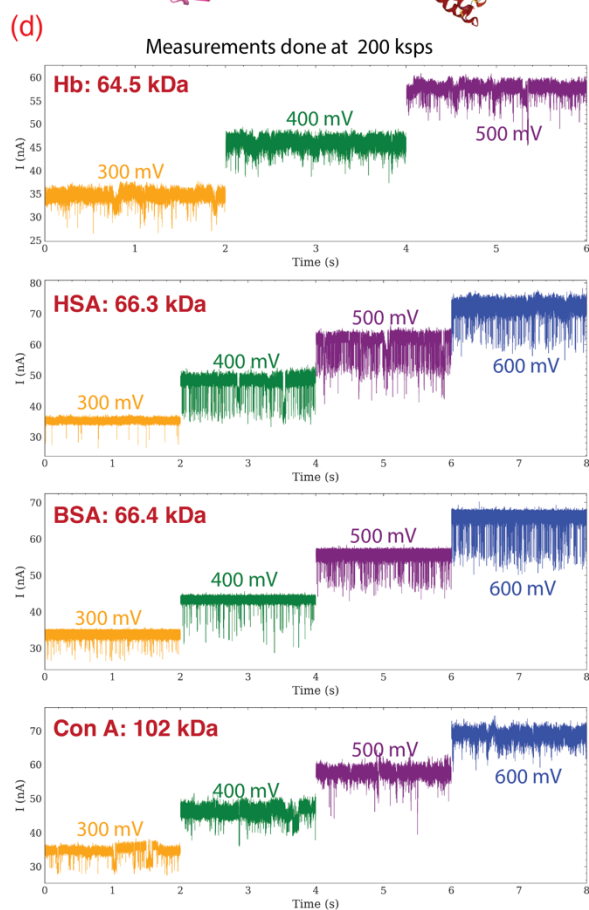
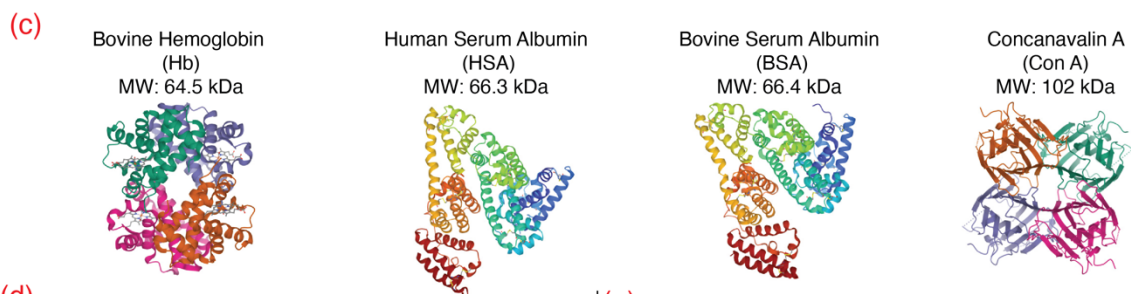
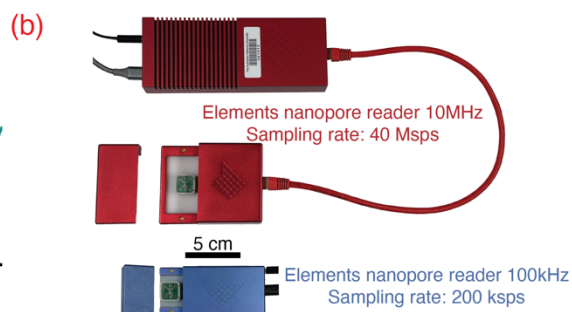
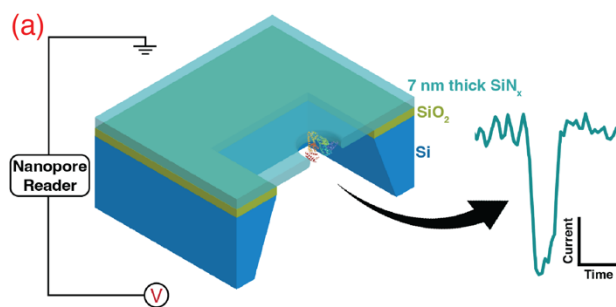
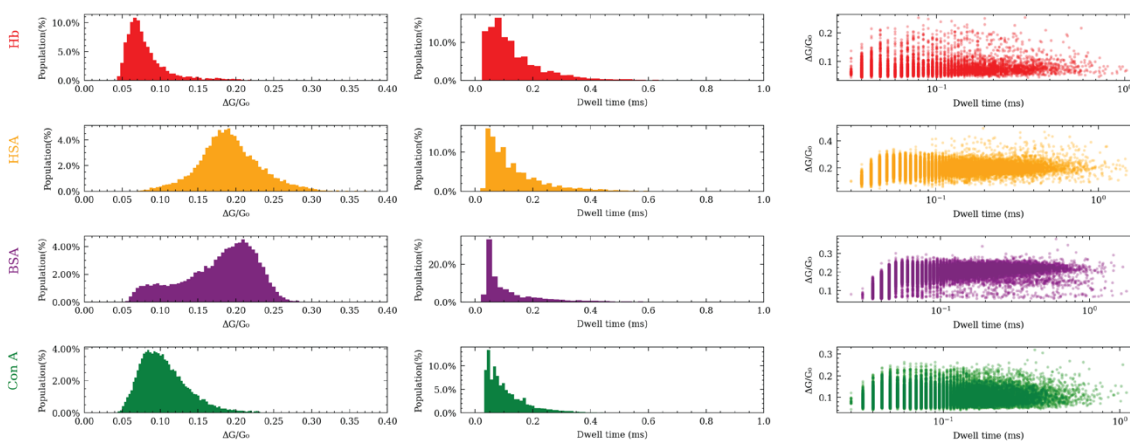
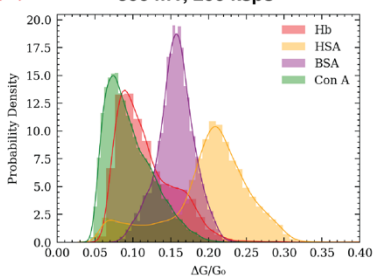


Figure 1: (a) Sketch of protein translocation through a SiNx nanopore membrane. The proteins (in a buffered electrolyte solution) are placed in the cis and trans channels depending on the charge and polarity of the applied voltage. Silver-silver chloride electrodes are used to apply a bias across the membrane. (b) Photographs of the portable amplifiers used for data acquisition: Elements 10MHz and 100kHz nanopore readers providing a sampling rate of 40 Msps and 200 ksps, respectively. (c) Different proteins used in the present study. Protein structures were obtained from the Protein Data Bank website of the Research Collaboratory for Structural Bioinformatics. (d), (e) Representative ionic current-time traces of different proteins under bias dc voltage ranging from 300 mV to 500 mV recorded at sampling rates of 200 ksps and 40 Msps, respectively. (f), (g) Event shape transformation showing the loss of detail during low-pass filtering: comparison of unfiltered signal and signal filtered at 35 kHz and 10 kHz frequencies (acquisition at 200 ksps) (f) and 1 MHz, 500 kHz, 100 kHz, and 35 kHz frequencies (acquisition at 40 Msps) (g).

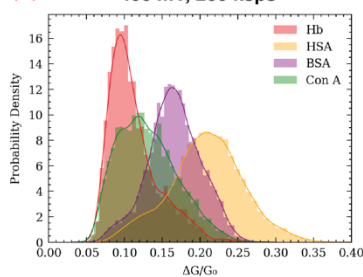
(a) Voltage Applied = 500 mV, Measured at 200 kps



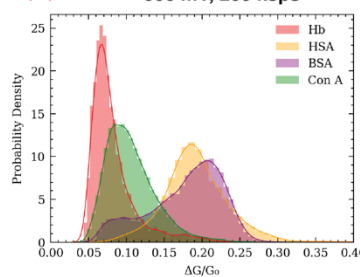
(b) 300 mV, 200 kps



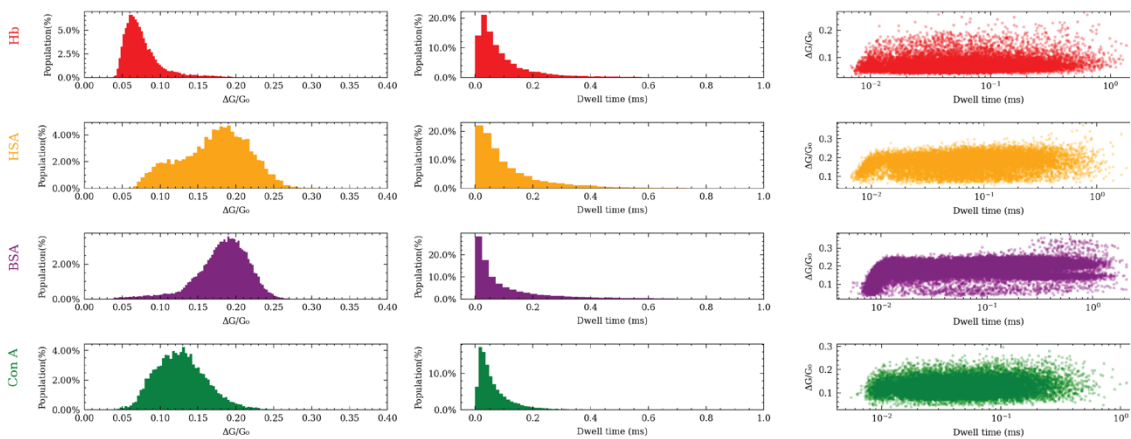
(c) 400 mV, 200 kps



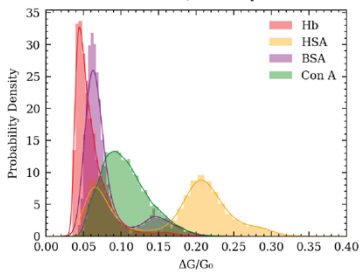
(d) 500 mV, 200 kps



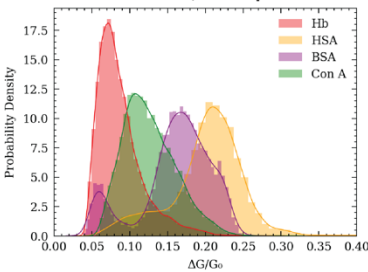
(e) Voltage Applied = 500 mV, Measured at 40 Mps



(f) 300 mV, 40 Mps



(g) 400 mV, 40 Mps



(h) 500 mV, 40 Mps

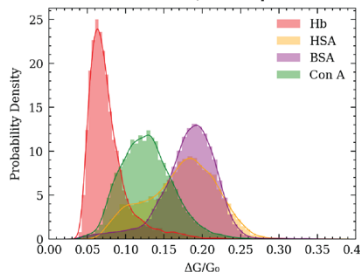


Figure 2: Histograms corresponding to the change in relative conductance ($\Delta G/G_0$), dwell time (Δt) as well as the scatter plots representing Δt as a function of $\Delta G/G_0$ for Hb, HSA, BSA, and Con A for measurements done using nanopore readers of bandwidths 100 kHz (a) and 10 MHz (e) with a cross-membrane bias of 500mV. The overlap of histograms corresponding to the change in relative conductance for measurements done at 200 ksps when at a cross-membrane bias of 300 mV (b), 400 mV(c) and 500 mV(d). For measurements taken at 40 Msps, overlapping histograms are displayed in (f), (g), and (h).

Figure 3: (a) Workflow for the label-free identification of proteins combining solid-state nanopores and machine learning. (b) Schematic displaying several resistive pulse feature parameters used for machine learning. Confusion matrices obtained for measurements taken at 200 ksps (c) and 40 Msps (d) using scheme 3 (cf. table 1). The applied bias was 500 mV. The darker the color in the matrix, the higher is the number of pulses corresponding to that combination. Identification accuracy in combinations of two, three and four different proteins for measurements done at sampling rates of 200kHz (e) and 40MHz (f). Orange represents combinations of two, green represents combinations of three, and purple shows combination of all four proteins. Under the same circumstances, measurements made at 40 Msps result in a greater overall accuracy of identification of a single protein among a mixture of four proteins.

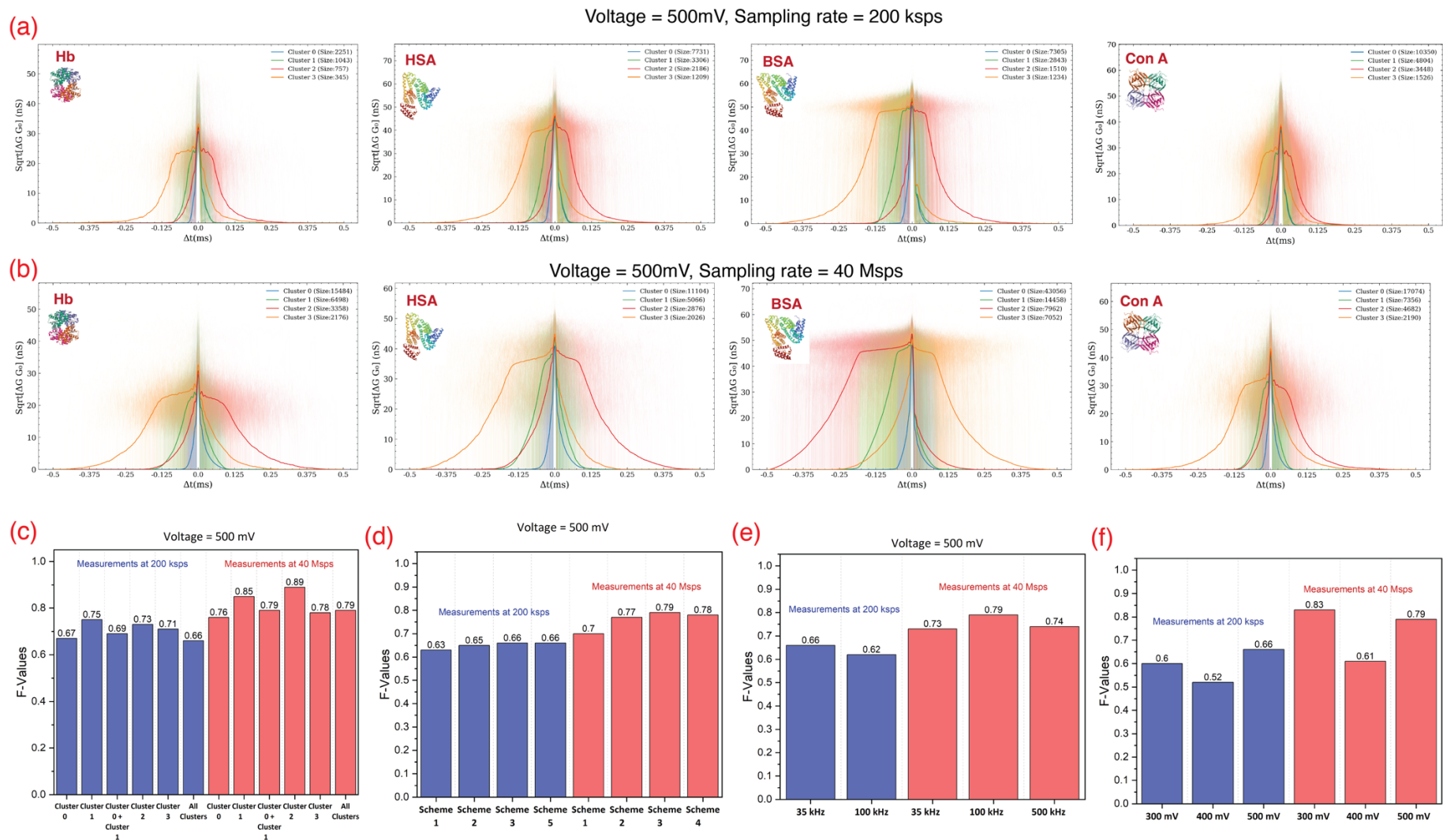


Figure 4: Splitting the signals into different clusters to differentiate between possible events (resulting from different conformations) as a protein molecule translocates through a nanopore for measurements performed at sampling rates of (a) 200 kps and (b) 40 Mps. The clusters shown are for measurements

with a trans-membrane bias of 500 mV. Due to surface charges on the nanopore wall and protein, specific and non-specific binding and interactions such as absorption, adsorption, electrostatic interaction etc, can lead to such different signals (c) Identification accuracy (for the case of combination of all four proteins) as a function of events corresponding to different clusters used for training the classification model. 500 mV was applied, and feature extraction was performed using scheme 3. Identification accuracy (for the case of combination of all four proteins, applied voltage = 500 mV) as a function of extraction scheme (d) and the cutoff frequency of the low pass filter used to filter the raw data (e). (f) Identification accuracy as a function of applied voltage during the measurements. The accuracy values depicted in (c)-(f) are color coded, i.e., blue for the measurements done at 200 ksps and red for measurements done at 40 Msps.

Table 1: Different feature extraction schemes and their corresponding features. The waveform was divided into n parts of width t_0/n and the average current drop corresponding to each part ($\Delta i_1, \Delta i_2, \dots \Delta i_n$) was used as an input. Other features include current drop at full width at half maximum (i_{fwhm}), the peak drop in current (i_{max}), width at full width at half maximum (t_{fwhm}), area of the waveform, skew and kurtosis. To account for the fluctuation in the nanopore size in different experiments, the values of the current characteristics were transformed into conductance and normalised by the open pore conductance.

Feature Extraction Scheme	Features/Details
Scheme 1	$\Delta i_1, \Delta i_2, \dots, \Delta i_{10} + t_0/10$
Scheme 2	$\Delta i_1, \Delta i_2, \dots \Delta i_{10} + t_0/10 + t_{fwhm} + \text{area} + i_{fwhm} + i_{max}$
Scheme 3	$\Delta i_1, \Delta i_2, \dots \Delta i_{10} + t_0/10 + t_{fwhm} + \text{area} + i_{fwhm} + i_{max} + \text{skew} + \text{kurtosis}$
Scheme 4	$\Delta i_1, \Delta i_2, \dots \Delta i_{50} + t_0/50 + t_{fwhm} + \text{area} + i_{fwhm} + i_{max} + \text{skew} + \text{kurtosis}$
Scheme 5	Full signal + $t_{fwhm} + \text{area} + i_{fwhm} + i_{max} + \text{skew} + \text{kurtosis}$

REFERENCES

- (1) Soto, C. Unfolding the Role of Protein Misfolding in Neurodegenerative Diseases. *Nat. Rev. Neurosci.* **2003**, *4* (1), 49–60. <https://doi.org/10.1038/nrn1007>.
- (2) Young, K. G.; Copeland, J. W. Formins in Cell Signaling. *Biochim. Biophys. Acta BBA - Mol. Cell Res.* **2010**, *1803* (2), 183–190. <https://doi.org/10.1016/j.bbamcr.2008.09.017>.
- (3) Eckersall, P. D.; Bell, R. Acute Phase Proteins: Biomarkers of Infection and Inflammation in Veterinary Medicine. *Vet. J.* **2010**, *185* (1), 23–27. <https://doi.org/10.1016/j.tvjl.2010.04.009>.
- (4) Hawkins, C. L.; Davies, M. J. Detection, Identification, and Quantification of Oxidative Protein Modifications. *J. Biol. Chem.* **2019**, *294* (51), 19683–19708. <https://doi.org/10.1074/jbc.REV119.006217>.
- (5) Buccitelli, C.; Selbach, M. MRNAs, Proteins and the Emerging Principles of Gene Expression Control. *Nat. Rev. Genet.* **2020**, *21* (10), 630–644. <https://doi.org/10.1038/s41576-020-0258-4>.
- (6) Scott, J. D.; Pawson, T. Cell Signaling in Space and Time: Where Proteins Come Together and When They're Apart. *Science* **2009**, *326* (5957), 1220–1224. <https://doi.org/10.1126/science.1175668>.
- (7) Chang, X.; Fang, K. PADI4 and Tumorigenesis. *Cancer Cell Int.* **2010**, *10*.
- (8) *Role of HIF-1 in Cancer Progression: Novel Insights. A Review: Ingenta Connect.* <https://www.ingentaconnect.com/content/ben/cmm/2018/00000018/00000006/art00001> (accessed 2023-02-20).
- (9) Semenza, G. L. Targeting HIF-1 for Cancer Therapy. *Nat. Rev. Cancer* **2003**, *3* (10), 721–732. <https://doi.org/10.1038/nrc1187>.
- (10) Naik, A. K.; Hanay, M. S.; Hiebert, W. K.; Feng, X. L.; Roukes, M. L. Towards Single-Molecule Nanomechanical Mass Spectrometry. *Nat. Nanotechnol.* **2009**, *4* (7), 445–450. <https://doi.org/10.1038/nnano.2009.152>.
- (11) Nedelkov, D.; Nelson, R. W. Surface Plasmon Resonance Mass Spectrometry: Recent Progress and Outlooks. *Trends Biotechnol.* **2003**, *21* (7), 301–305. [https://doi.org/10.1016/S0167-7799\(03\)00141-0](https://doi.org/10.1016/S0167-7799(03)00141-0).
- (12) Rule, G. S.; Hitchens, T. K. *Fundamentals of Protein NMR Spectroscopy*; Springer Science & Business Media, 2006.

- (13) Jia, C.-P.; Zhong, X.-Q.; Hua, B.; Liu, M.-Y.; Jing, F.-X.; Lou, X.-H.; Yao, S.-H.; Xiang, J.-Q.; Jin, Q.-H.; Zhao, J.-L. Nano-ELISA for Highly Sensitive Protein Detection. *Biosens. Bioelectron.* **2009**, *24* (9), 2836–2841. <https://doi.org/10.1016/j.bios.2009.02.024>.
- (14) Kaboord, B.; Perr, M. Isolation of Proteins and Protein Complexes by Immunoprecipitation. In *2D PAGE: Sample Preparation and Fractionation*; Posch, A., Ed.; Methods in Molecular BiologyTM; Humana Press: Totowa, NJ, 2008; pp 349–364. https://doi.org/10.1007/978-1-60327-064-9_27.
- (15) Maveyraud, L.; Mourey, L. Protein X-Ray Crystallography and Drug Discovery. *Molecules* **2020**, *25* (5), 1030. <https://doi.org/10.3390/molecules25051030>.
- (16) Piston, D. W.; Kremers, G.-J. Fluorescent Protein FRET: The Good, the Bad and the Ugly. *Trends Biochem. Sci.* **2007**, *32* (9), 407–414. <https://doi.org/10.1016/j.tibs.2007.08.003>.
- (17) Rosenstein, J. K.; Wanunu, M.; Merchant, C. A.; Drndic, M.; Shepard, K. L. Integrated Nanopore Sensing Platform with Sub-Microsecond Temporal Resolution. *Nat. Methods* **2012**, *9* (5), 487–492. <https://doi.org/10.1038/nmeth.1932>.
- (18) Smeets, R. M. M.; Keyser, U. F.; Krapf, D.; Wu, M.-Y.; Dekker, N. H.; Dekker, C. Salt Dependence of Ion Transport and DNA Translocation through Solid-State Nanopores. *Nano Lett.* **2006**, *6* (1), 89–95. <https://doi.org/10.1021/nl052107w>.
- (19) Plesa, C.; Kowalczyk, S. W.; Zinsmeister, R.; Grosberg, A. Y.; Rabin, Y.; Dekker, C. Fast Translocation of Proteins through Solid State Nanopores. *Nano Lett.* **2013**, *13* (2), 658–663. <https://doi.org/10.1021/nl3042678>.
- (20) Wei, R.; Gatterdam, V.; Wieneke, R.; Tampé, R.; Rant, U. Stochastic Sensing of Proteins with Receptor-Modified Solid-State Nanopores. *Nat. Nanotechnol.* **2012**, *7* (4), 257–263. <https://doi.org/10.1038/nnano.2012.24>.
- (21) Im, J.; Lindsay, S.; Wang, X.; Zhang, P. Single Molecule Identification and Quantification of Glycosaminoglycans Using Solid-State Nanopores. *ACS Nano* **2019**, *13* (6), 6308–6318. <https://doi.org/10.1021/acsnano.9b00618>.
- (22) Karawdeniya, B. I.; Bandara, Y. M. N. D. Y.; Nichols, J. W.; Chevalier, R. B.; Dwyer, J. R. Surveying Silicon Nitride Nanopores for Glycomics and Heparin Quality Assurance. *Nat. Commun.* **2018**, *9* (1), 3278. <https://doi.org/10.1038/s41467-018-05751-y>.
- (23) Taniguchi, M.; Minami, S.; Ono, C.; Hamajima, R.; Morimura, A.; Hamaguchi, S.; Akeda, Y.; Kanai, Y.; Kobayashi, T.; Kamitani, W.; Terada, Y.; Suzuki, K.; Hatori, N.;

- Yamagishi, Y.; Washizu, N.; Takei, H.; Sakamoto, O.; Naono, N.; Tatematsu, K.; Washio, T.; Matsuura, Y.; Tomono, K. Combining Machine Learning and Nanopore Construction Creates an Artificial Intelligence Nanopore for Coronavirus Detection. *Nat. Commun.* **2021**, *12* (1), 3726. <https://doi.org/10.1038/s41467-021-24001-2>.
- (24) Arima, A.; Tsutsui, M.; Washio, T.; Baba, Y.; Kawai, T. Solid-State Nanopore Platform Integrated with Machine Learning for Digital Diagnosis of Virus Infection. *Anal. Chem.* **2021**, *93* (1), 215–227. <https://doi.org/10.1021/acs.analchem.0c04353>.
- (25) Goyal, G.; Darvish, A.; Jun Kim, M. Use of Solid-State Nanopores for Sensing Co-Translocational Deformation of Nano-Liposomes. *Analyst* **2015**, *140* (14), 4865–4873. <https://doi.org/10.1039/C5AN00250H>.
- (26) Hu, R.; Rodrigues, J. V.; Waduge, P.; Yamazaki, H.; Cressiot, B.; Chishti, Y.; Makowski, L.; Yu, D.; Shakhnovich, E.; Zhao, Q.; Wanunu, M. Differential Enzyme Flexibility Probed Using Solid-State Nanopores. *ACS Nano* **2018**, *12* (5), 4494–4502. <https://doi.org/10.1021/acsnano.8b00734>.
- (27) Li, J.; Fologea, D.; Rollings, R.; Ledden, B. Characterization of Protein Unfolding with Solid-State Nanopores. *Protein Pept. Lett.* **2014**, *21* (3), 256–265.
- (28) Bandara, Y. M. N. D. Y.; Freedman, K. J. Enhanced Signal to Noise Ratio Enables High Bandwidth Nanopore Recordings and Molecular Weight Profiling of Proteins. *ACS Nano* **2022**, *16* (9), 14111–14120. <https://doi.org/10.1021/acsnano.2c04046>.
- (29) Sha, J.; Si, W.; Xu, B.; Zhang, S.; Li, K.; Lin, K.; Shi, H.; Chen, Y. Identification of Spherical and Nonspherical Proteins by a Solid-State Nanopore. *Anal. Chem.* **2018**, *90* (23), 13826–13831. <https://doi.org/10.1021/acs.analchem.8b04136>.
- (30) Kwak, D.-K.; Chae, H.; Lee, M.-K.; Ha, J.-H.; Goyal, G.; Kim, M. J.; Kim, K.-B.; Chi, S.-W. Probing the Small-Molecule Inhibition of an Anticancer Therapeutic Protein-Protein Interaction Using a Solid-State Nanopore. *Angew. Chem. Int. Ed.* **2016**, *55* (19), 5713–5717. <https://doi.org/10.1002/anie.201511601>.
- (31) Lin, C.-Y.; Fotis, R.; Xia, Z.; Kavetsky, K.; Chou, Y.-C.; Niedzwiecki, D. J.; Biondi, M.; Thei, F.; Drndić, M. Ultrafast Polymer Dynamics through a Nanopore. *Nano Lett.* **2022**, *22* (21), 8719–8727. <https://doi.org/10.1021/acsnanolett.2c03546>.
- (32) Larkin, J.; Henley, R. Y.; Muthukumar, M.; Rosenstein, J. K.; Wanunu, M. High-Bandwidth Protein Analysis Using Solid-State Nanopores. *Biophys. J.* **2014**, *106* (3), 696–704. <https://doi.org/10.1016/j.bpj.2013.12.025>.
- (33) Chien, C.-C.; Shekar, S.; Niedzwiecki, D. J.; Shepard, K. L.; Drndić, M. Single-Stranded DNA Translocation Recordings through Solid-State Nanopores on Glass Chips

- at 10 MHz Measurement Bandwidth. *ACS Nano* **2019**, *13* (9), 10545–10554.
<https://doi.org/10.1021/acsnano.9b04626>.
- (34) Freedman, K. J.; Bastian, A. R.; Chaiken, I.; Kim, M. J. Solid-State Nanopore Detection of Protein Complexes: Applications in Healthcare and Protein Kinetics. *Small* **2013**, *9* (5), 750–759. <https://doi.org/10.1002/smll.201201423>.
- (35) Fahie, M.; Chisholm, C.; Chen, M. Resolved Single-Molecule Detection of Individual Species within a Mixture of Anti-Biotin Antibodies Using an Engineered Monomeric Nanopore. *ACS Nano* **2015**, *9* (2), 1089–1098. <https://doi.org/10.1021/nn506606e>.
- (36) Wan, Y. K.; Hendra, C.; Pratanwanich, P. N.; Göke, J. Beyond Sequencing: Machine Learning Algorithms Extract Biology Hidden in Nanopore Signal Data. *Trends Genet.* **2021**, S0168952521002572. <https://doi.org/10.1016/j.tig.2021.09.001>.
- (37) Xia, K.; Hagan, J. T.; Fu, L.; Sheetz, B. S.; Bhattacharya, S.; Zhang, F.; Dwyer, J. R.; Linhardt, R. J. Synthetic Heparan Sulfate Standards and Machine Learning Facilitate the Development of Solid-State Nanopore Analysis. *Proc. Natl. Acad. Sci.* **2021**, *118* (11), e2022806118. <https://doi.org/10.1073/pnas.2022806118>.
- (38) Tsutsui, M.; Yoshida, T.; Yokota, K.; Yasaki, H.; Yasui, T.; Arima, A.; Tonomura, W.; Nagashima, K.; Yanagida, T.; Kaji, N.; Taniguchi, M.; Washio, T.; Baba, Y.; Kawai, T. Discriminating Single-Bacterial Shape Using Low-Aspect-Ratio Pores. *Sci. Rep.* **2017**, *7* (1), 17371. <https://doi.org/10.1038/s41598-017-17443-6>.
- (39) *Discrimination of α -Thrombin and γ -Thrombin Using Aptamer-Functionalized Nanopore Sensing | Analytical Chemistry.*
<https://pubs.acs.org/doi/full/10.1021/acs.analchem.1c00461> (accessed 2023-02-20).
- (40) Smeets, R. M. M.; Keyser, U. F.; Dekker, N. H.; Dekker, C. Noise in Solid-State Nanopores. *Proc. Natl. Acad. Sci.* **2008**, *105* (2), 417–421.
<https://doi.org/10.1073/pnas.0705349105>.
- (41) Lee, K.; Park, K.-B.; Kim, H.-J.; Yu, J.-S.; Chae, H.; Kim, H.-M.; Kim, K.-B. Recent Progress in Solid-State Nanopores. *Adv. Mater.* **2018**, *30* (42), 1704680.
<https://doi.org/10.1002/adma.201704680>.
- (42) Goto, Y.; Yanagi, I.; Matsui, K.; Yokoi, T.; Takeda, K. Integrated Solid-State Nanopore Platform for Nanopore Fabrication via Dielectric Breakdown, DNA-Speed Deceleration and Noise Reduction. *Sci. Rep.* **2016**, *6* (1), 31324. <https://doi.org/10.1038/srep31324>.
- (43) Dutt, S.; Karawdeniya, B. I.; Bandara, Y. M. N. D. Y.; Kluth, P. Controlled Fabrication of Thin Silicon Nitride Membranes for Nanopore Sensing. arXiv January 22, 2022.
<https://doi.org/10.48550/arXiv.2201.09024>.

- (44) Waugh, M.; Briggs, K.; Gunn, D.; Gibeault, M.; King, S.; Ingram, Q.; Jimenez, A. M.; Berryman, S.; Lomovtsev, D.; Andrzejewski, L.; Tabard-Cossa, V. Solid-State Nanopore Fabrication by Automated Controlled Breakdown. *Nat. Protoc.* **2020**, *15* (1), 122–143. <https://doi.org/10.1038/s41596-019-0255-2>.
- (45) Kwok, H.; Briggs, K.; Tabard-Cossa, V. Nanopore Fabrication by Controlled Dielectric Breakdown. *PLoS ONE* **2014**, *9* (3), e92880–e92880. <https://doi.org/10/f53dj6>.
- (46) Likas, A.; Vlassis, N.; J. Verbeek, J. The Global K-Means Clustering Algorithm. *Pattern Recognit.* **2003**, *36* (2), 451–461. [https://doi.org/10.1016/S0031-3203\(02\)00060-2](https://doi.org/10.1016/S0031-3203(02)00060-2).
- (47) Biau, G.; Scornet, E. A Random Forest Guided Tour. *TEST* **2016**, *25* (2), 197–227. <https://doi.org/10.1007/s11749-016-0481-7>.
- (48) Rodriguez, J. J.; Kuncheva, L. I.; Alonso, C. J. Rotation Forest: A New Classifier Ensemble Method. *IEEE Trans. Pattern Anal. Mach. Intell.* **2006**, *28* (10), 1619–1630. <https://doi.org/10.1109/TPAMI.2006.211>.
- (49) Taniguchi, M. Combination of Single-Molecule Electrical Measurements and Machine Learning for the Identification of Single Biomolecules. *ACS Omega* **2020**, *5* (2), 959–964. <https://doi.org/10.1021/acsomega.9b03660>.
- (50) Pedregosa, F.; Varoquaux, G.; Gramfort, A.; Michel, V.; Thirion, B.; Grisel, O.; Blondel, M.; Prettenhofer, P.; Weiss, R.; Dubourg, V.; Vanderplas, J.; Passos, A.; Cournapeau, D.; Brucher, M.; Perrot, M.; Duchesnay, É. Scikit-Learn: Machine Learning in Python. *J. Mach. Learn. Res.* **2011**, *12* (85), 2825–2830.

SUPPLEMENTARY INFORMATION

Table S1: List and details of proteins used in this study. The approximate values for the isoelectric points (pI) were obtained from the manufacturer or from other easily accessible data sources.

Protein	Product Details	MW	Isoelectric point
Bovine Hemoglobin (Hb)	Sigma Aldrich, H2500	64.5 kDa	7.1
Human Serum Albumin (HSA)	Sigma Aldrich, A9511	66.3 kDa	4.7
Bovine Serum Albumin (BSA)	Sigma Aldrich, A2153	66.4 kDa	4.6
Concanavalin A (Con A)	Sigma Aldrich, C2010	102 kDa	4.9

Table S2: Characteristics (open pore conductance (G_0) using 1 M KCl, pH~7, calculated pore diameter and protein measurement done) of the nanopores used to measure proteins. Results in the main text are shown corresponding to Chip ID of CHN139, CHN122, CHN121 and CHN118.

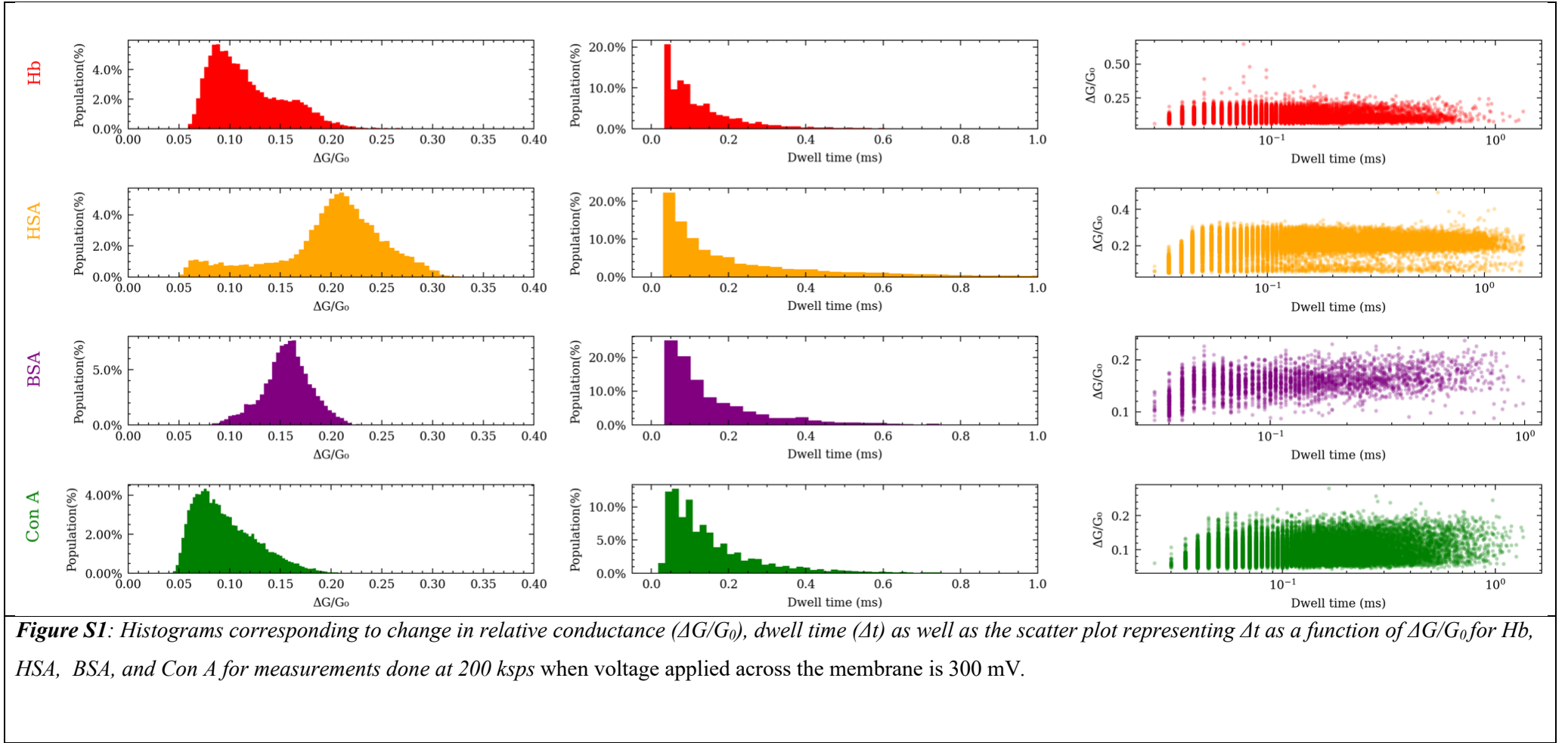
Chip ID	Protein Measured	G_0 (nS)	Calculated Pore Diameter
CHN139	Hb	111 ± 2	16.1 ± 0.4
CHN119	Hb	105 ± 1	15.5 ± 0.3
CHN122	HSA	103 ± 3	15.3 ± 0.4
CHN121	Con A	116 ± 1	16.6 ± 0.3

CHN72	Con A	102 \pm 1	15.1 \pm 0.3
CHN118	BSA	117 \pm 2	16.8 \pm 0.4
CHN64	BSA	105 \pm 1	15.5 \pm 0.3
CHN116	BSA	104 \pm 2	15.4 \pm 0.4

Table S3: Number of waveforms obtained from different measurements at different voltages for different proteins corresponding to Chip ID of CHN139, CHN122, CHN121 and CHN118.

Protein	Voltage Applied (mV)	Number of waveforms extracted (measured at 200 ksp/s)	Number of waveforms extracted (measured at 40 Msps)
Hb	300	18,003	32,149
	400	4,330	57,097
	500	8,320	17,504
HSA	300	39,552	64,310
	400	27,325	32,644
	500	39,345	24,810
	600	40,580	-

BSA	300	7,605	8,034
	400	19,563	22,653
	500	29,509	62,066
	600	24,186	-
Con A	300	35,908	16,778
	400	18,992	21,095
	500	58,312	21,925
	600	40,004	-



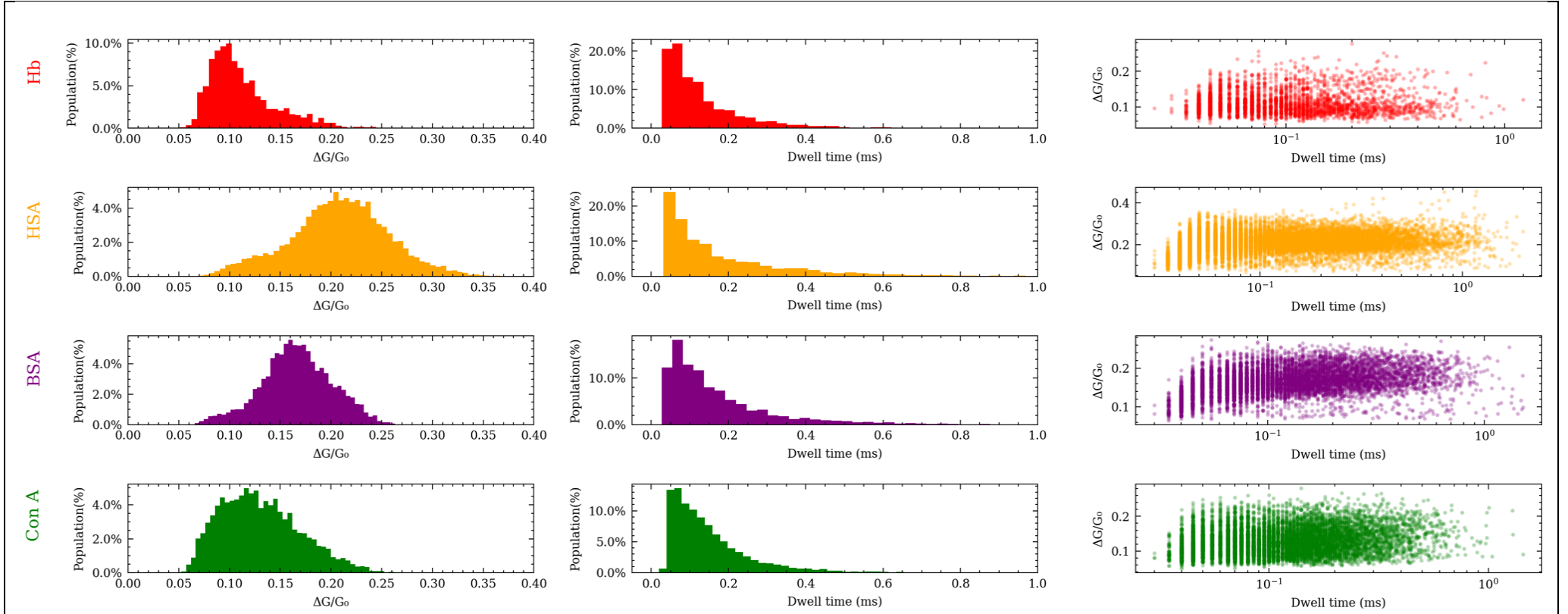
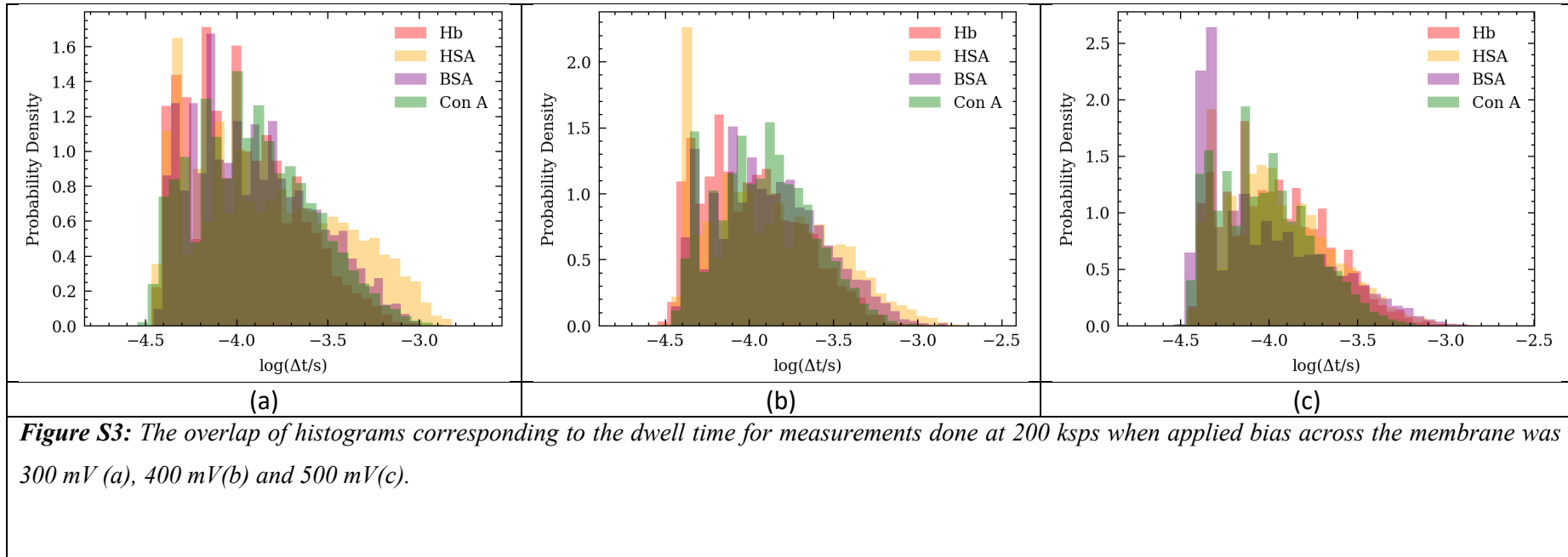


Figure S2: Histograms corresponding to change in relative conductance ($\Delta G/G_0$), dwell time (Δt) as well as the scatter plot representing Δt as a function of $\Delta G/G_0$ for Hb, HSA, BSA, and Con A for measurements done at 200 kps when voltage applied across the membrane is 400 mV.

a



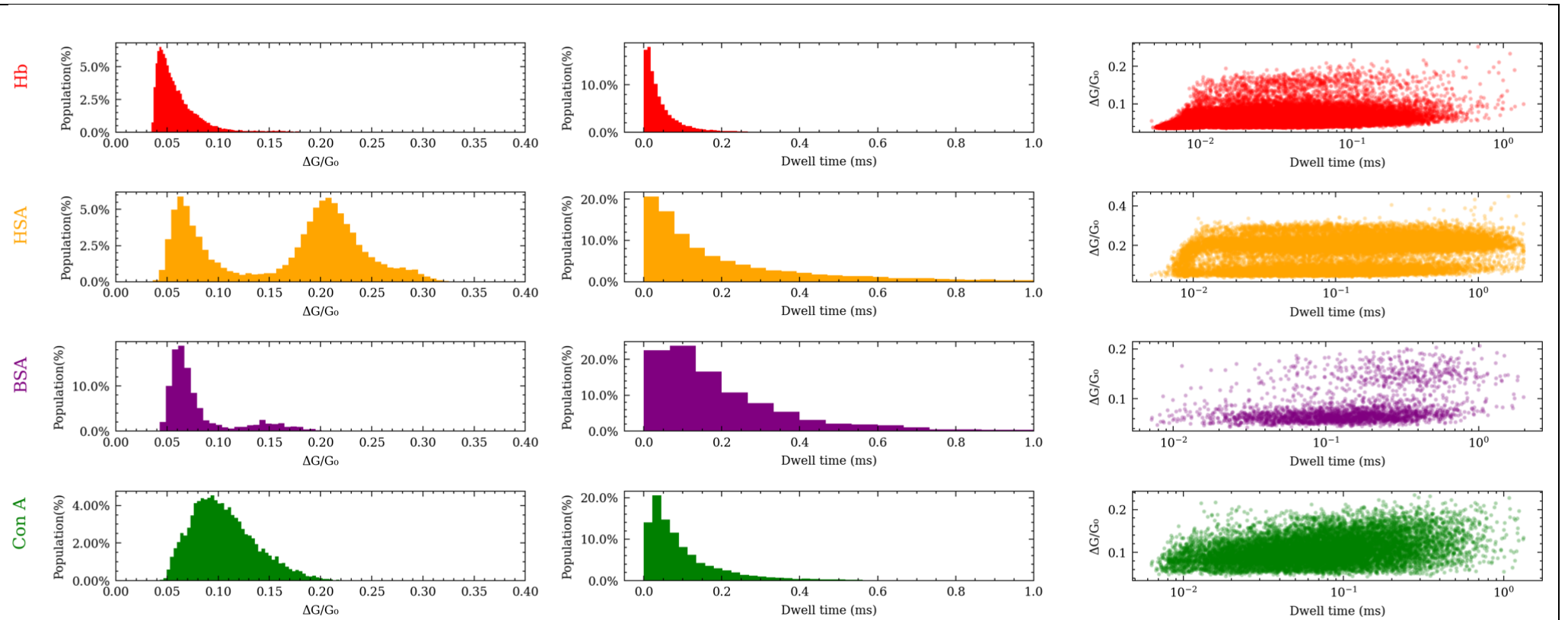
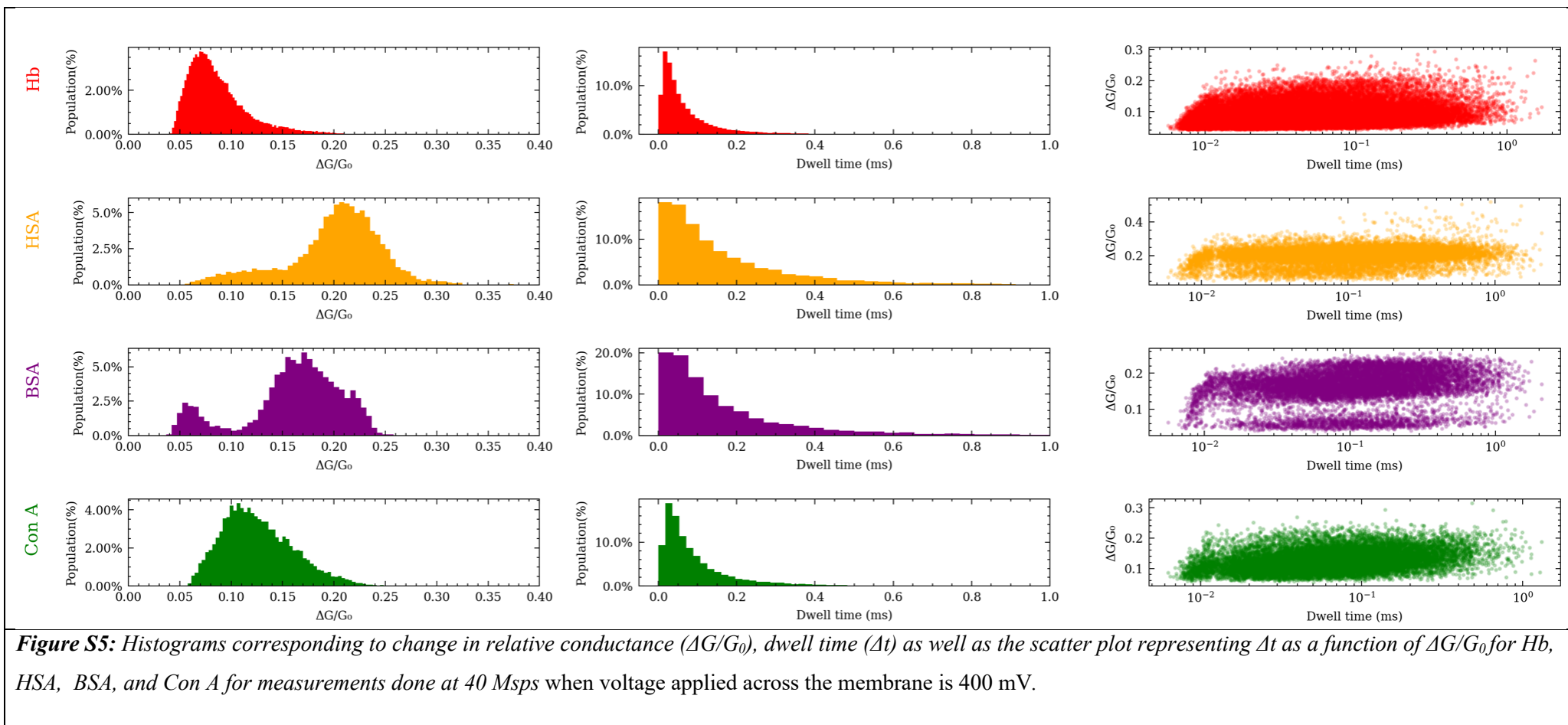


Figure S4: Histograms corresponding to change in relative conductance ($\Delta G/G_0$), dwell time (Δt) as well as the scatter plot representing Δt as a function of $\Delta G/G_0$ for Hb, HSA, BSA, and Con A for measurements done at 40 Msps when voltage applied across the membrane is 300 mV.



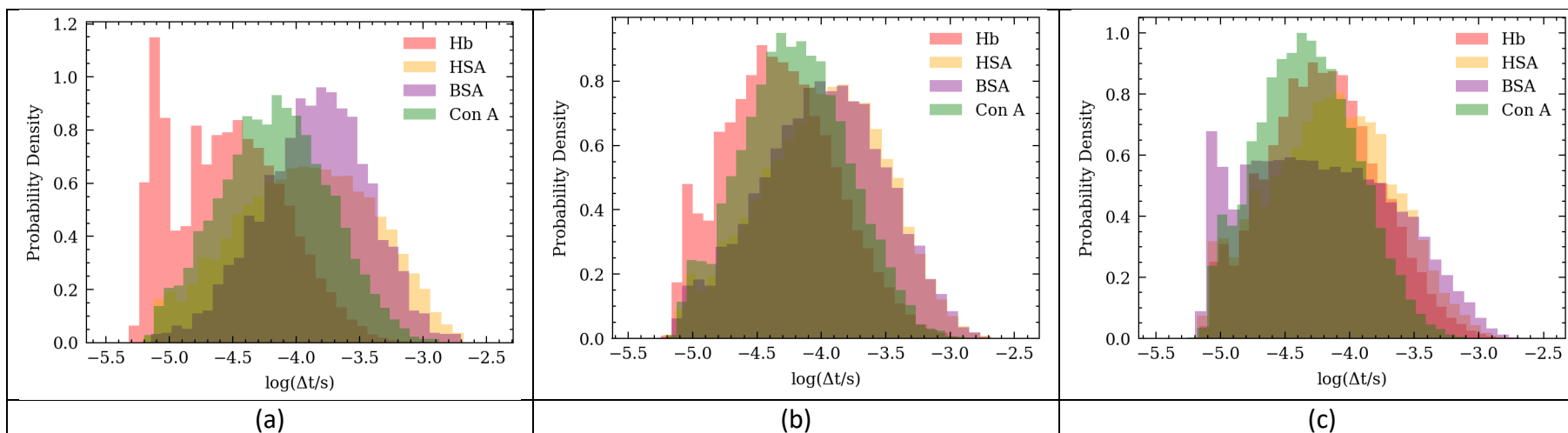


Figure S6: The overlap of histograms corresponding to the dwell time for measurements done at 40 Msps when applied bias across the membrane was 300 mV (a), 400 mV (b) and 500 mV (c).

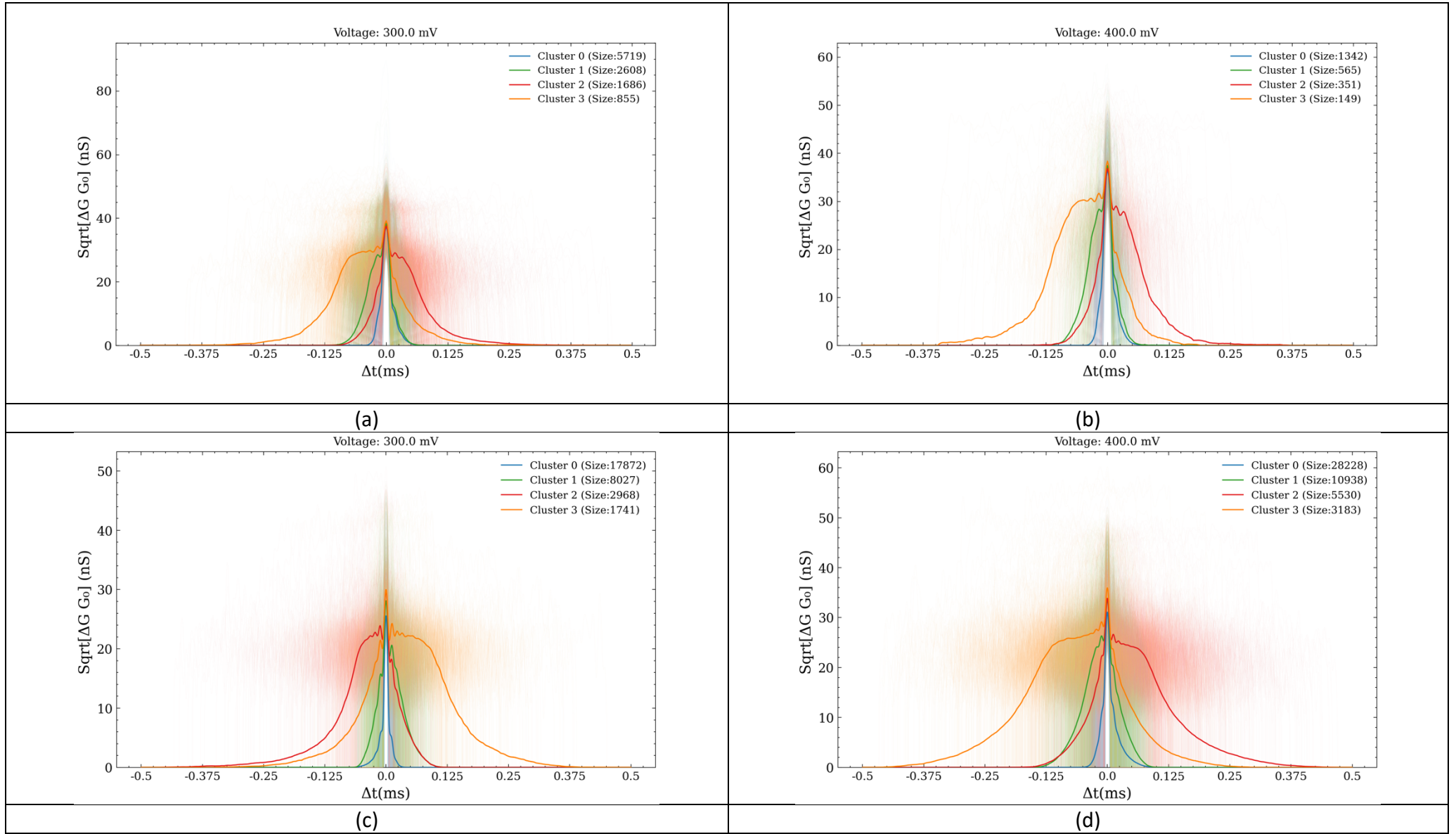


Figure S7: Clustering the signals into different clusters to differentiate possible translocation events from one another as Hb translocates through a nanopore. The clusters are shown for measurements done at 200 kps under the applied bias of 300 mV (a) and 400 mV (b). Also shown are clusters resulting from measurements done at 40 Msps under the applied bias of 300 mV (c) and 400 mV (d).

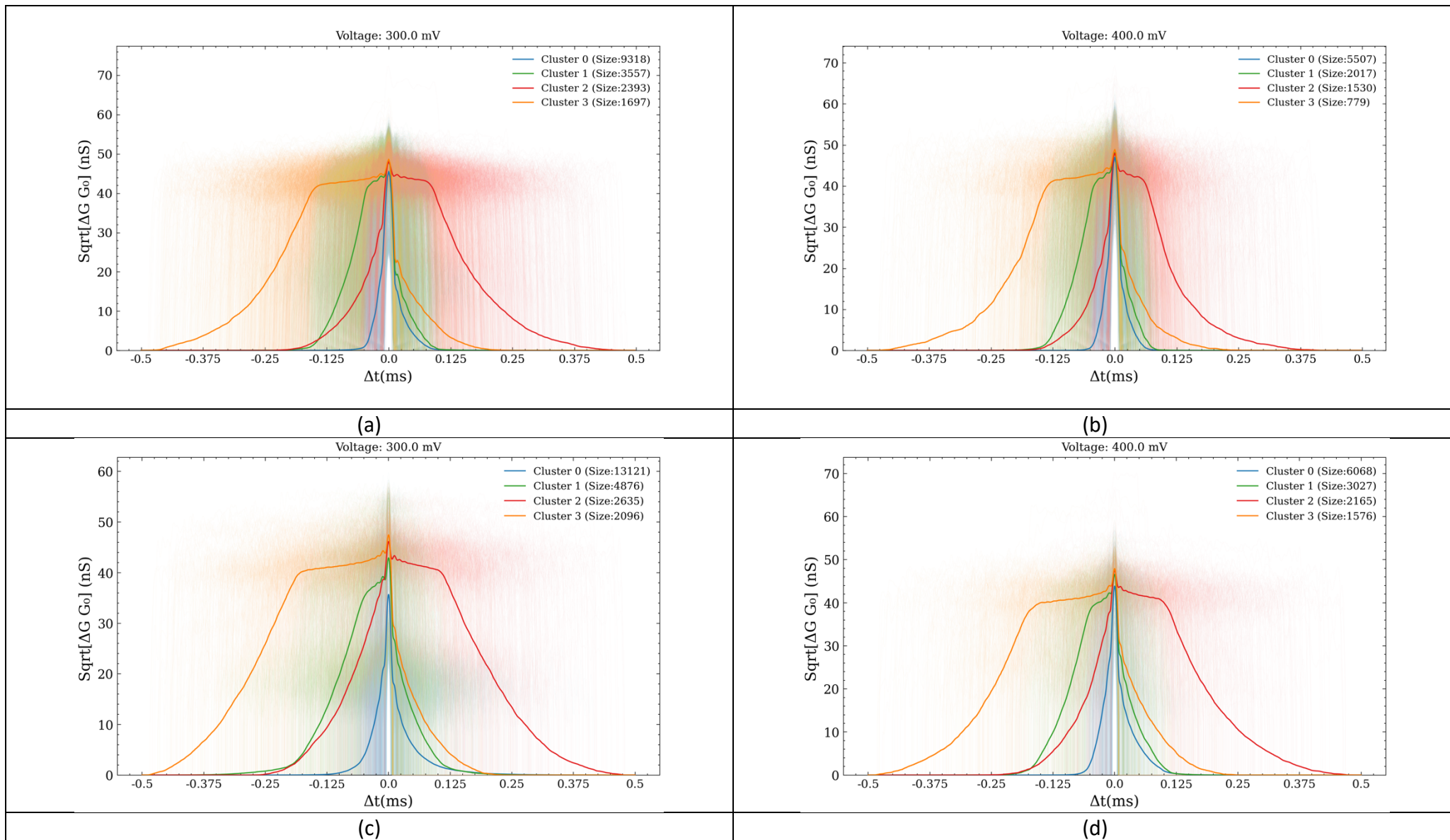


Figure S8: Clustering the signals into different clusters to differentiate possible translocation events from one another as HSA translocates through a nanopore. The clusters are shown for measurements done at 200 kps under the applied bias of 300 mV (a) and 400 mV (b). Also shown are clusters resulting from measurements done at 40 Mps under the applied bias of 300 mV (c) and 400 mV (d).

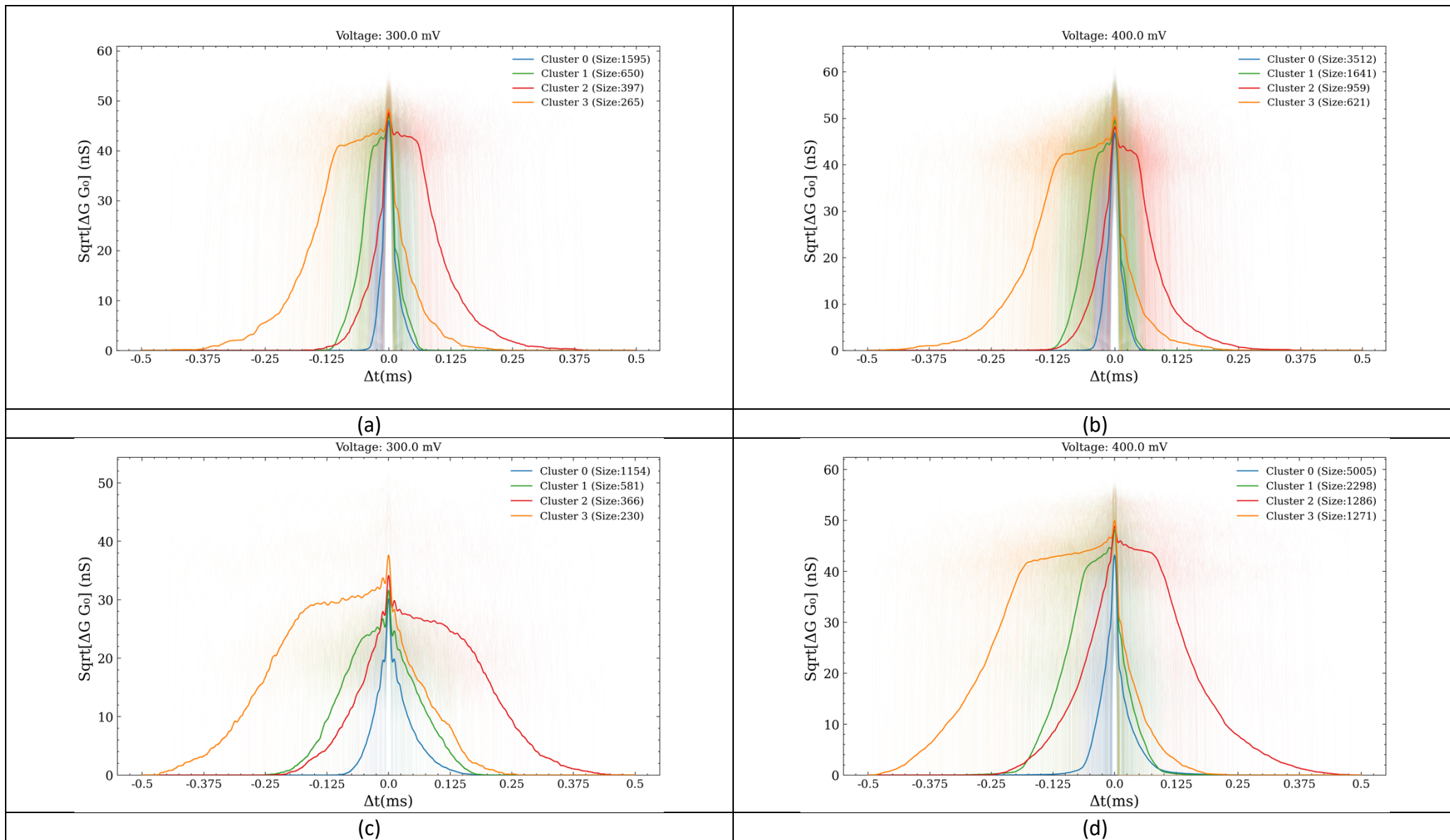
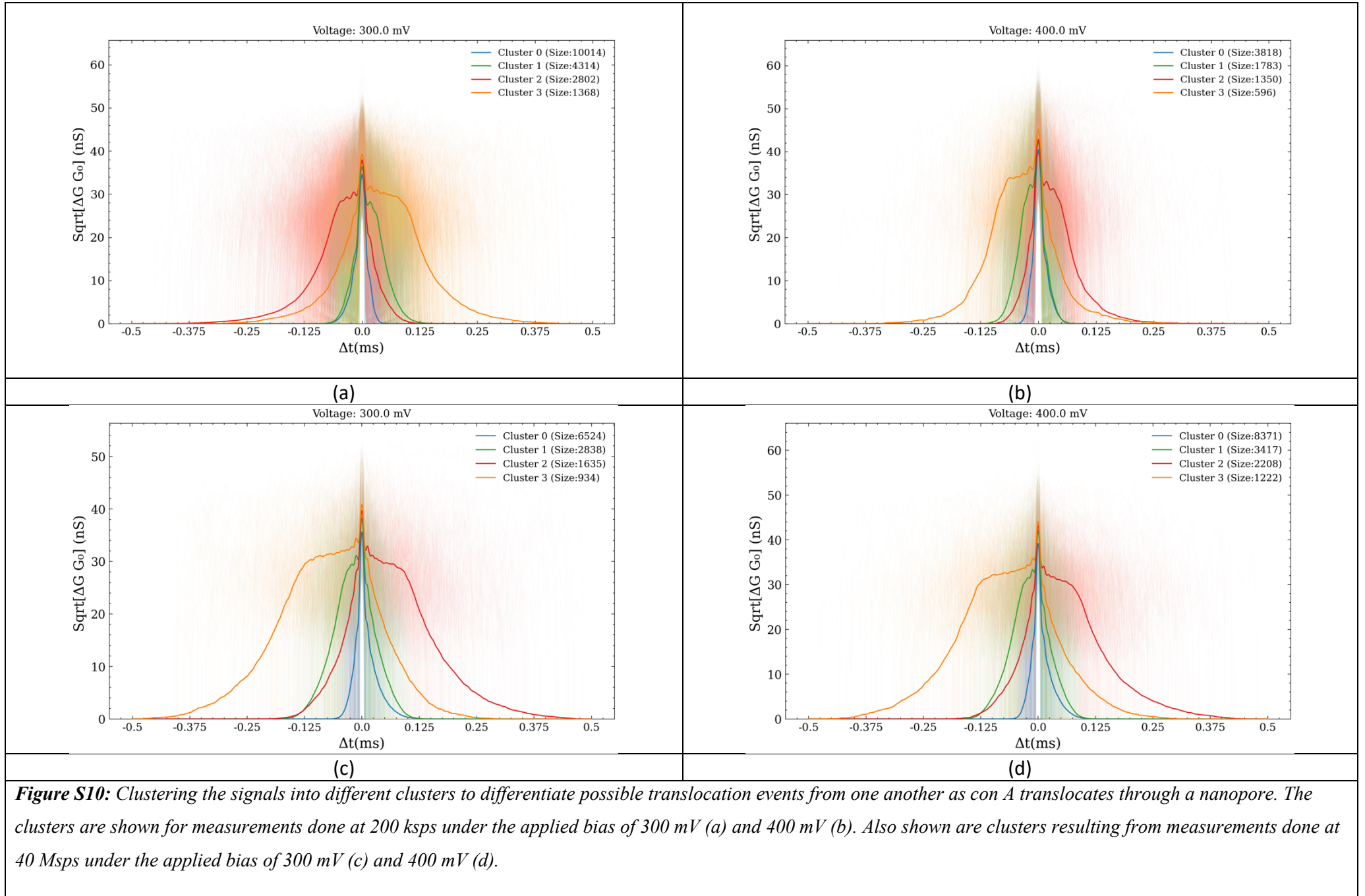
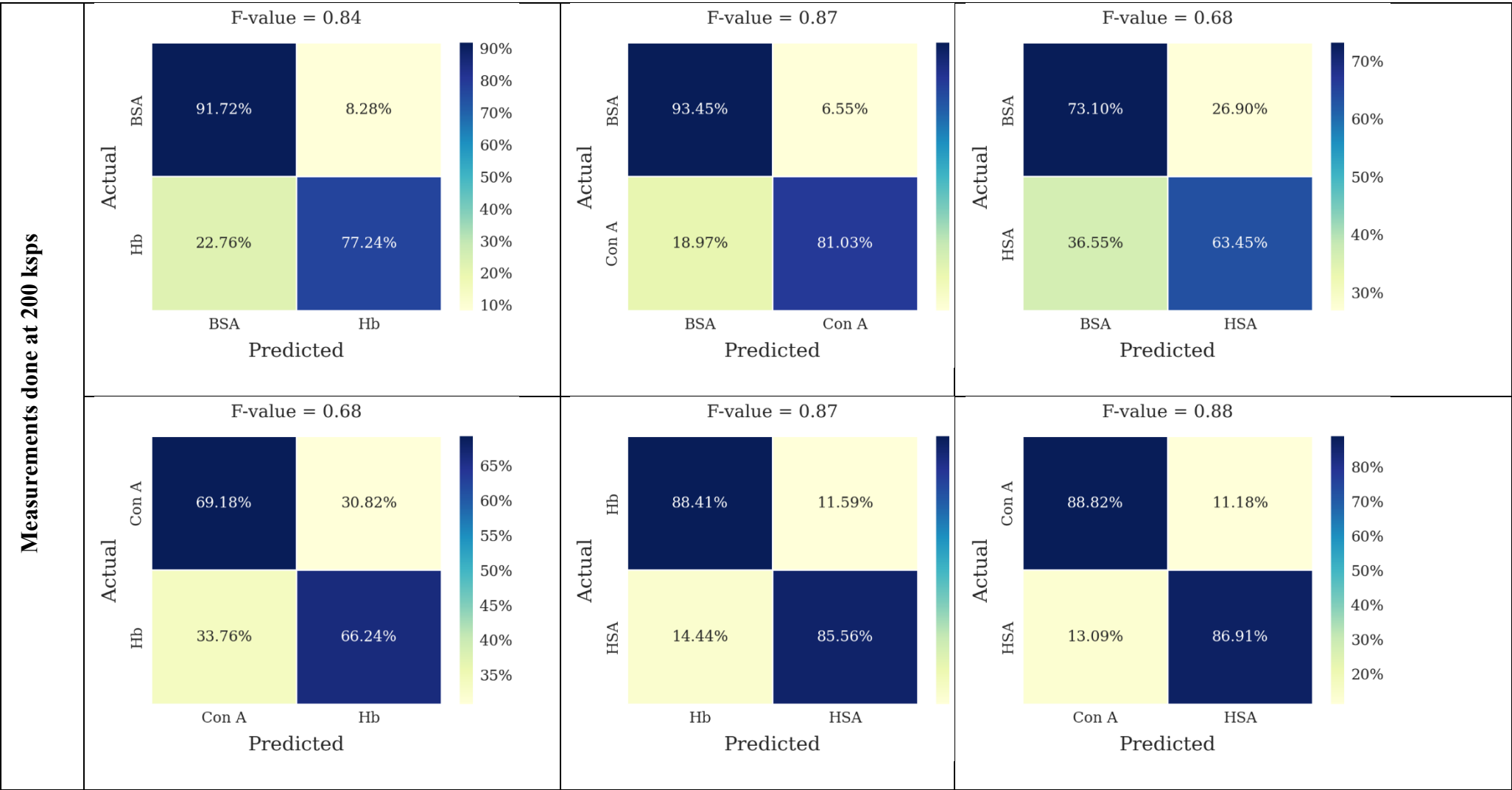
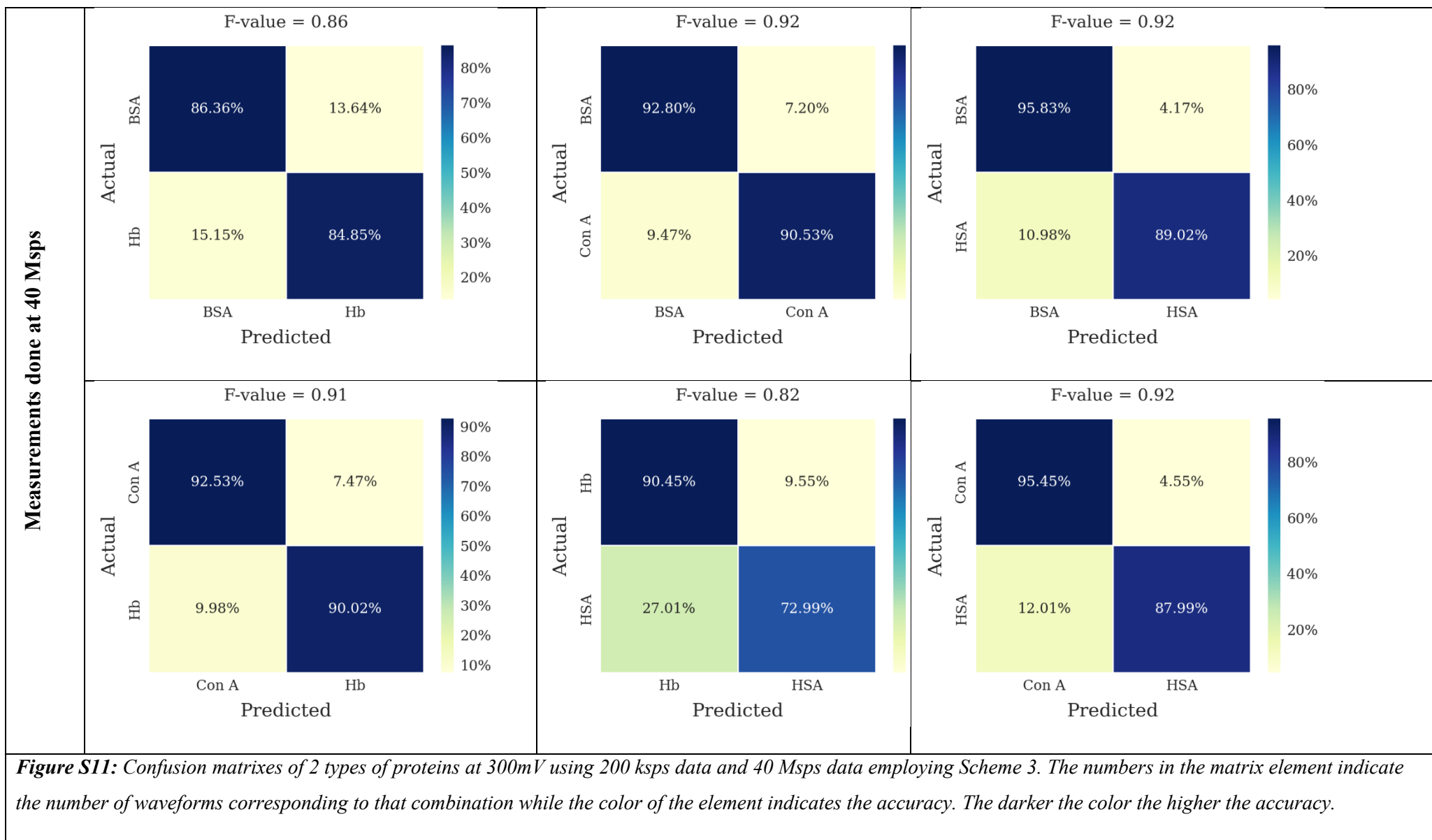
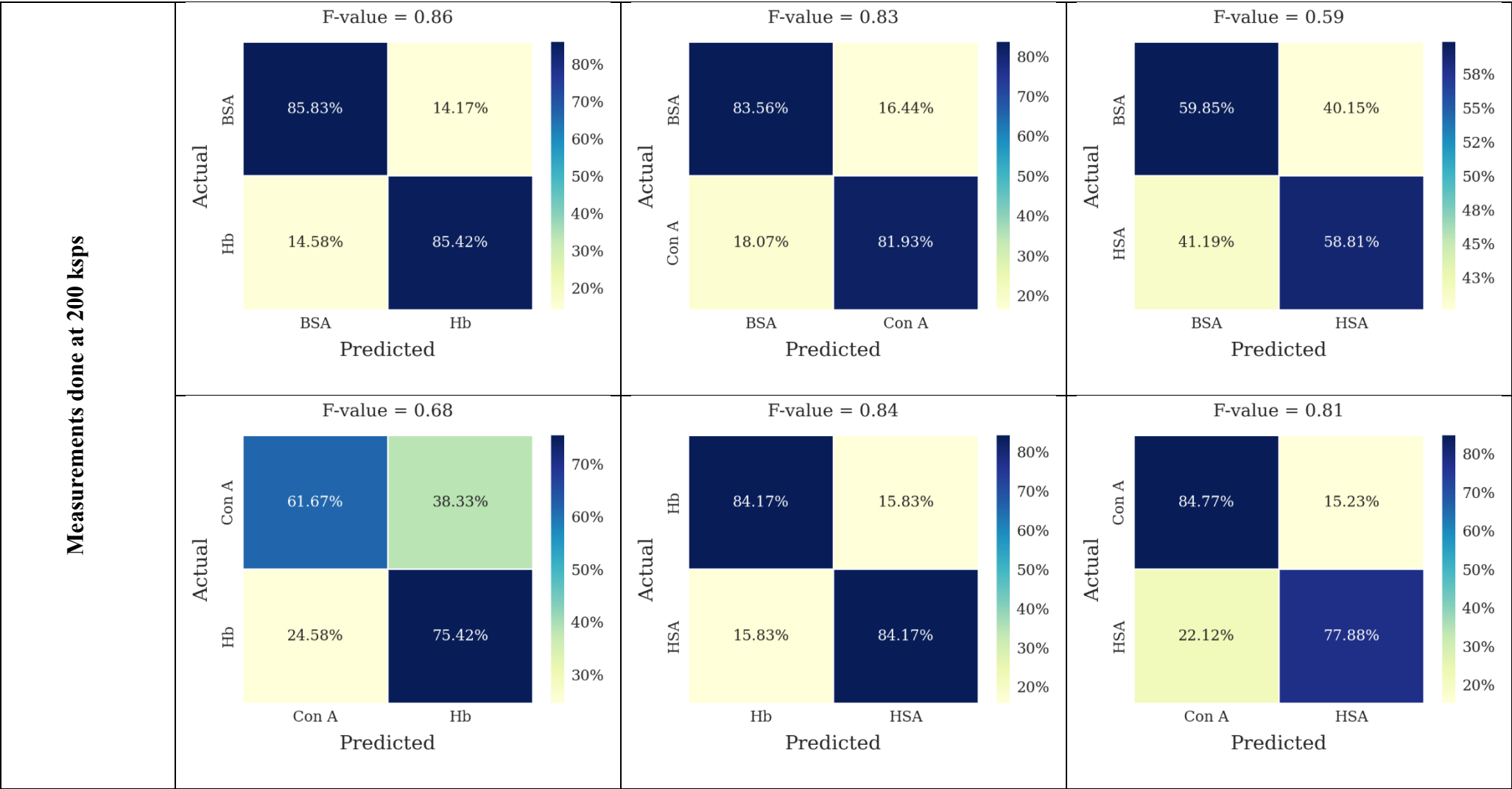


Figure S9: Clustering the signals into different clusters to differentiate possible translocation events from one another as BSA translocates through a nanopore. The clusters are shown for measurements done at 200 kps under the applied bias of 300 mV (a) and 400 mV (b). Also shown are clusters resulting from measurements done at 40 Mps under the applied bias of 300 mV (c) and 400 mV (d).









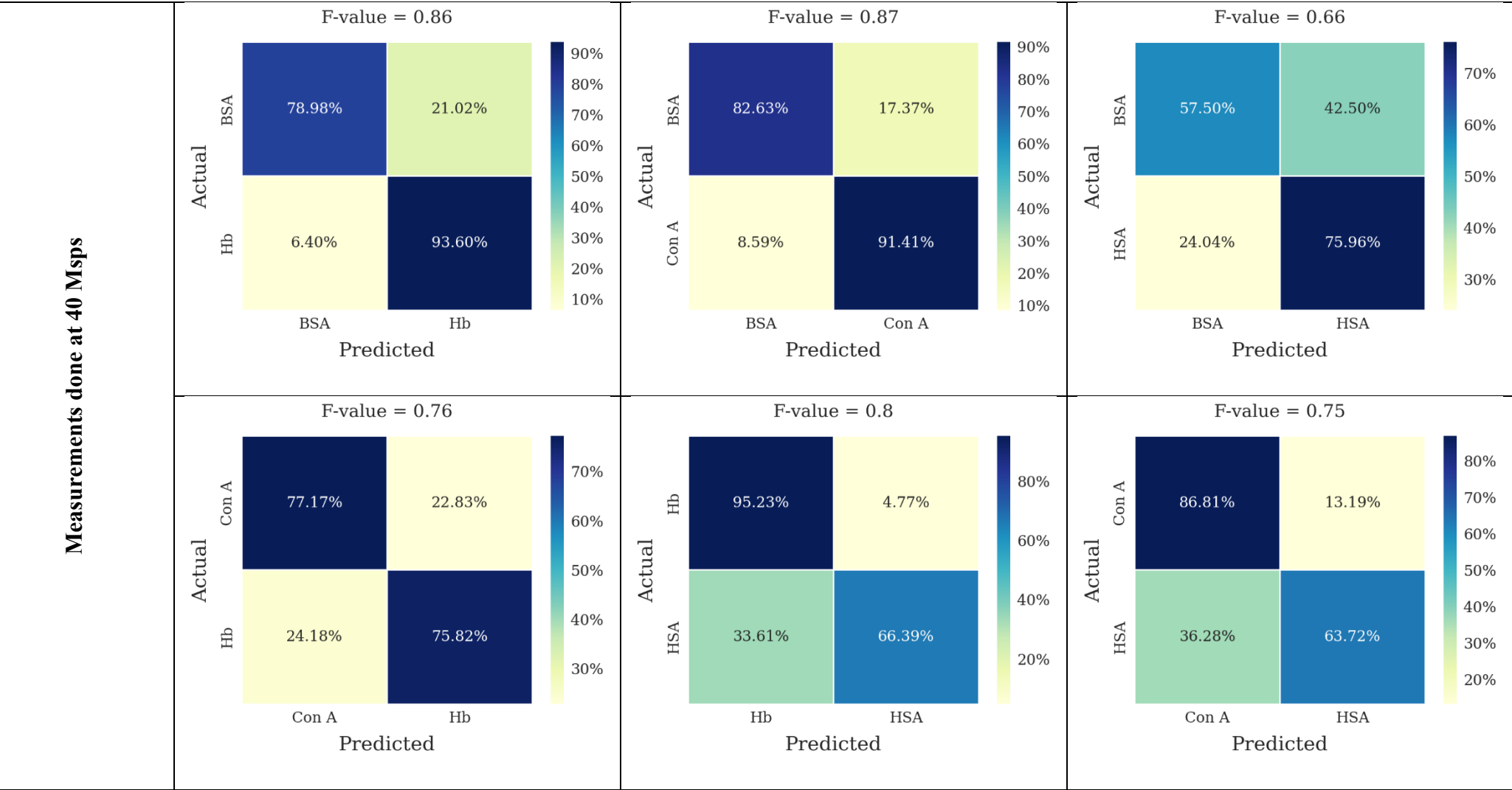
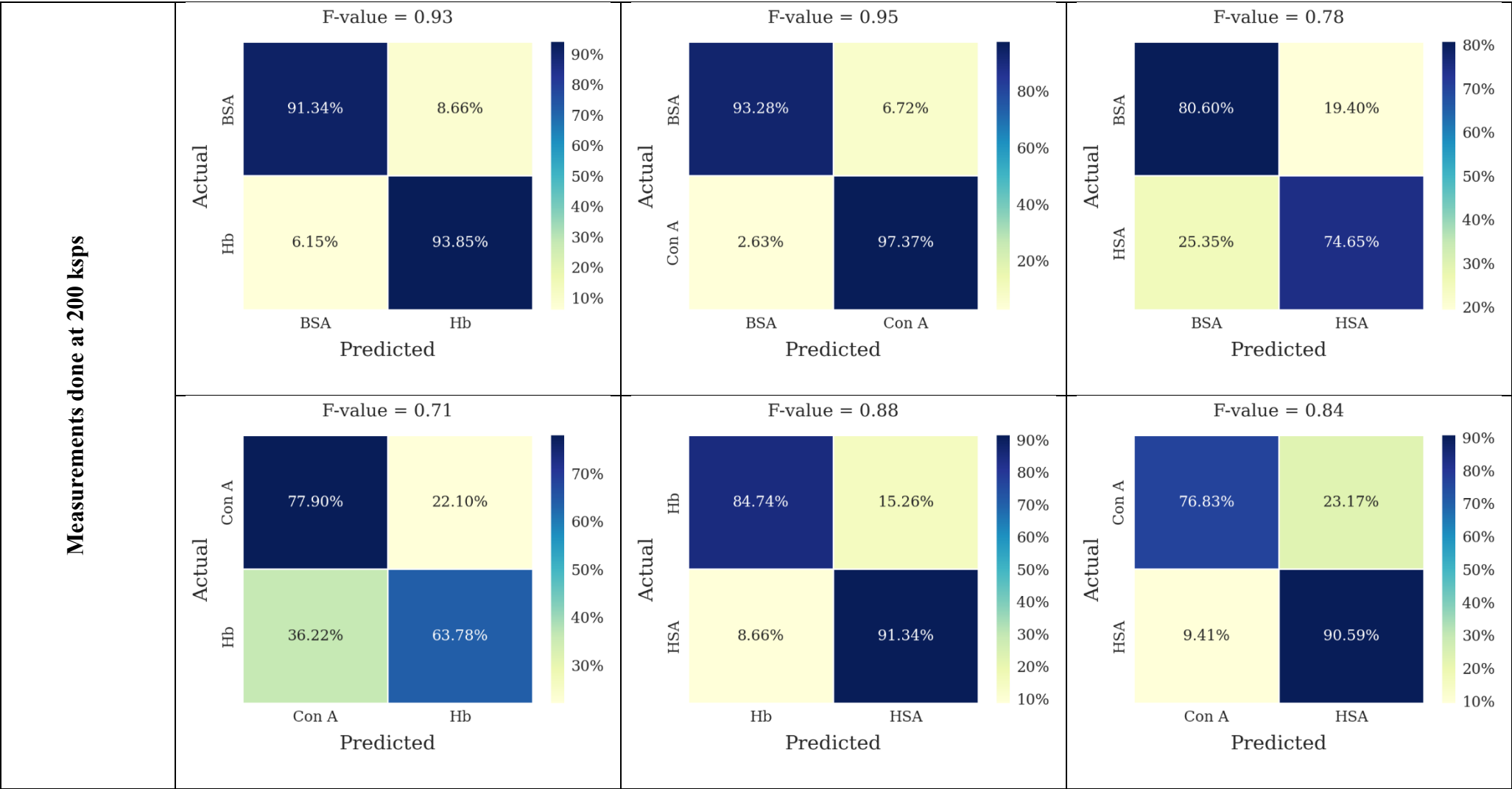


Figure S12: Confusion matrixes of 2 types of proteins at 400mV using 200 kps data and 40 Msps data employing Scheme 3. The numbers in the matrix element indicate the number of waveforms corresponding to that combination while the color of the element indicates the accuracy. The darker the color the higher the accuracy.



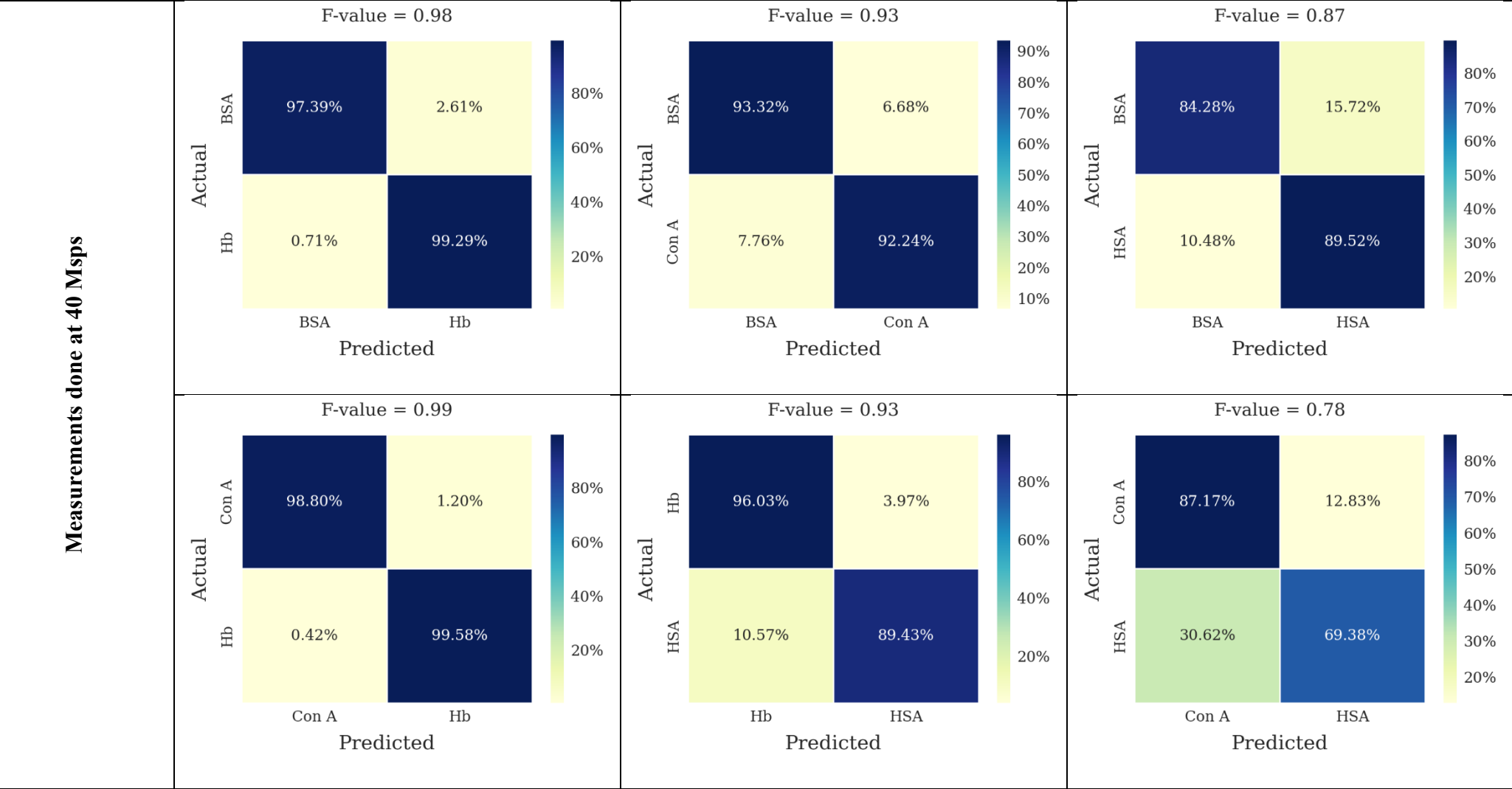
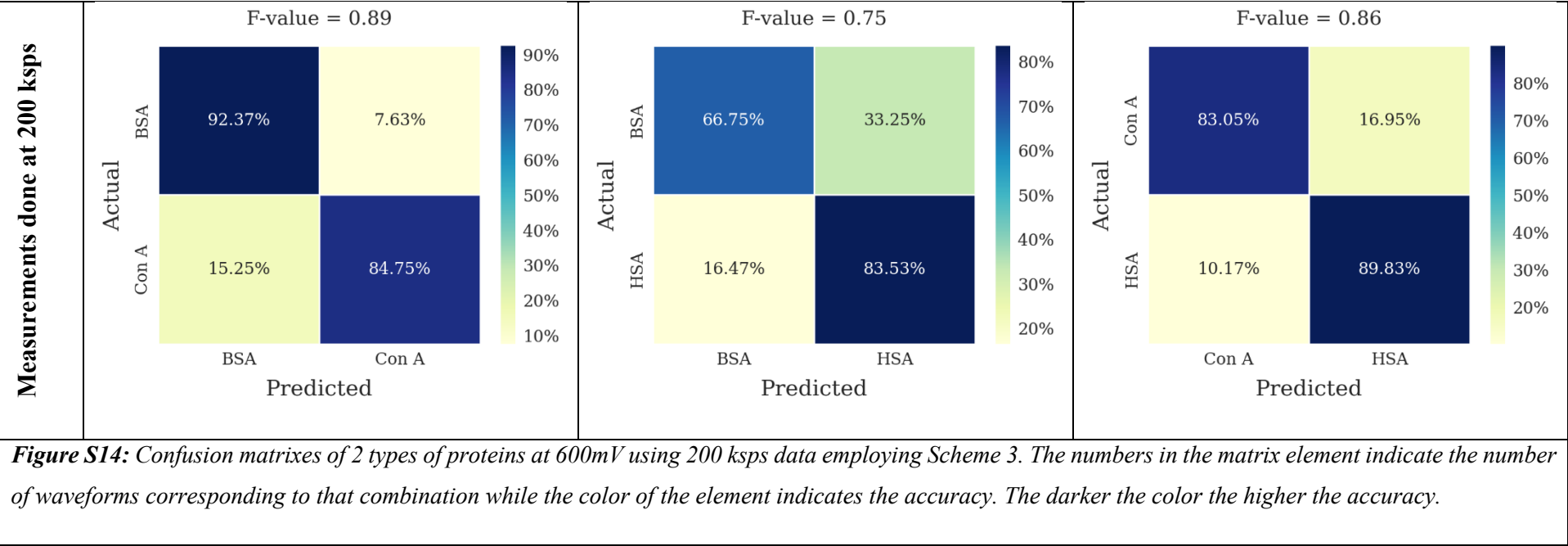
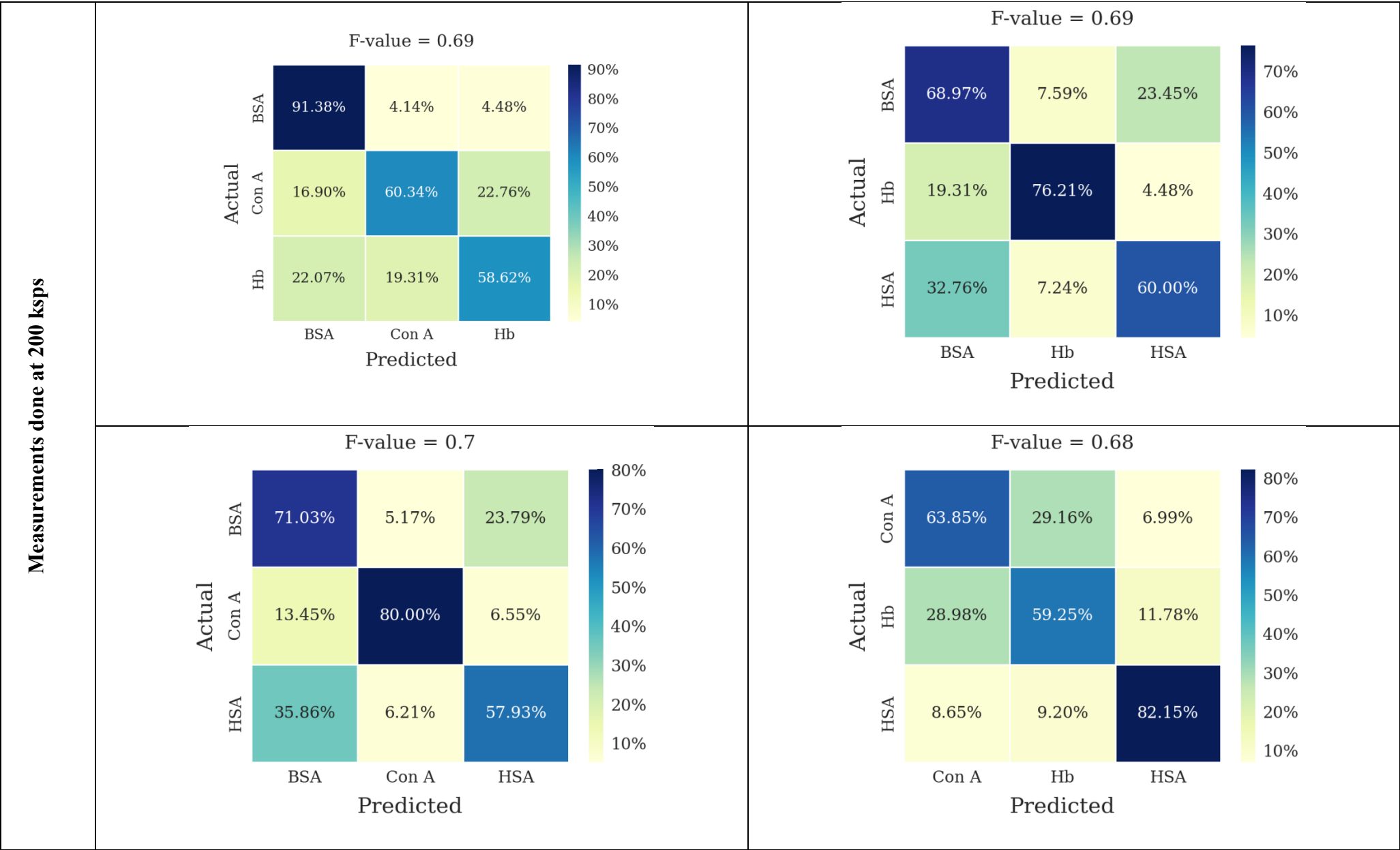
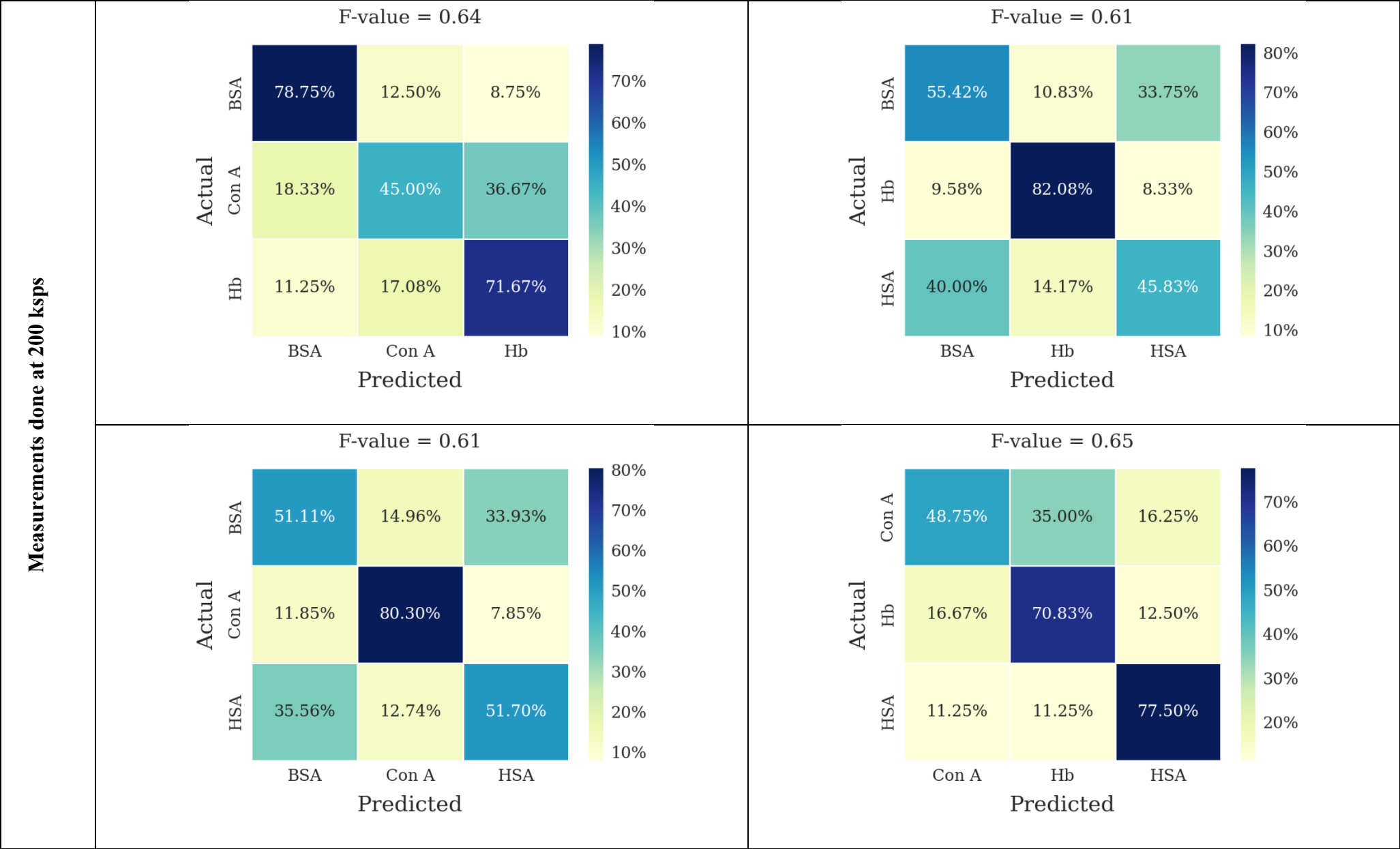


Figure S13: Confusion matrixes of 2 types of proteins at 500mV using 200 kps data and 40 Msps data employing Scheme 3. The numbers in the matrix element indicate the number of waveforms corresponding to that combination while the color of the element indicates the accuracy. The darker the color the higher the accuracy.









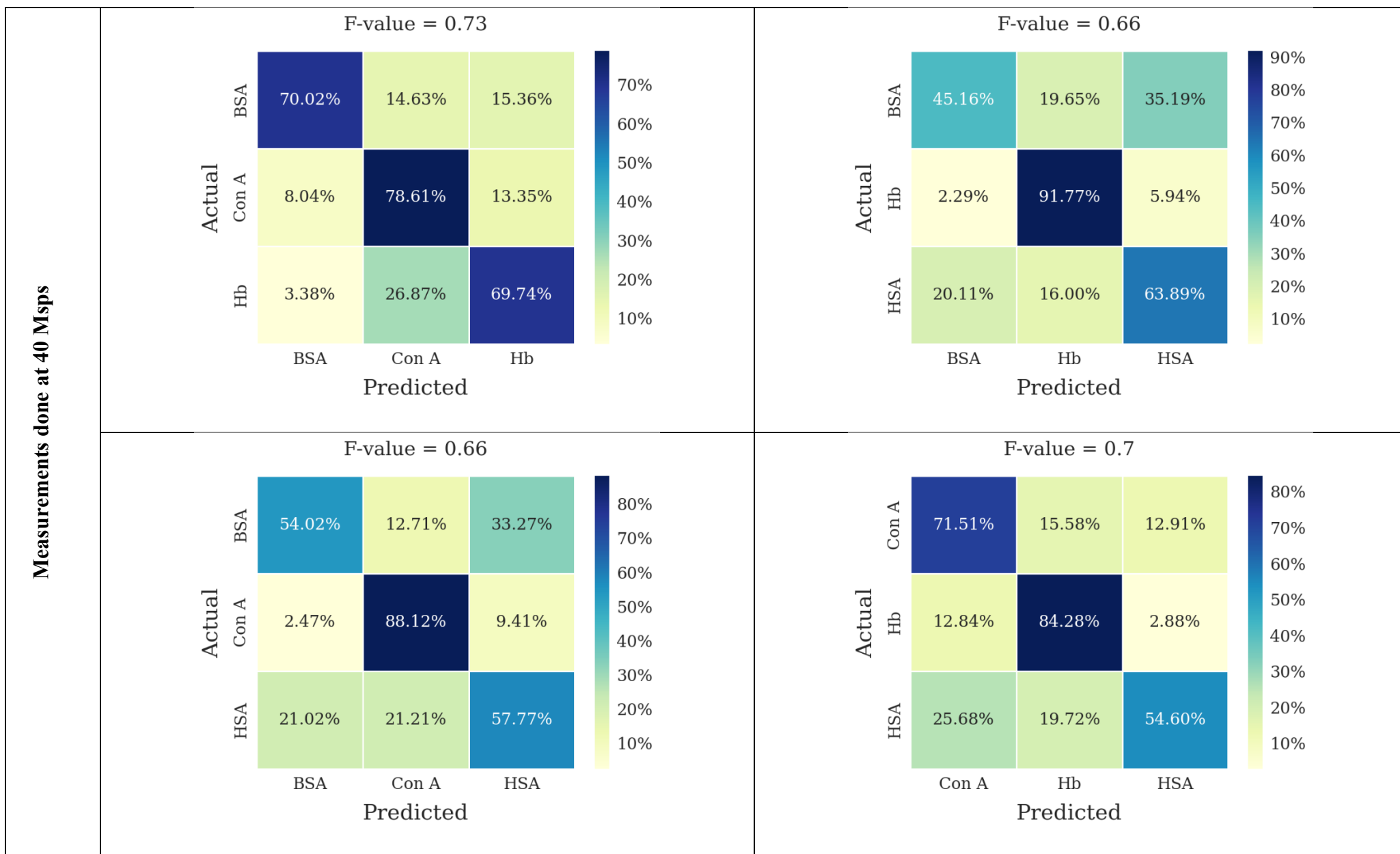
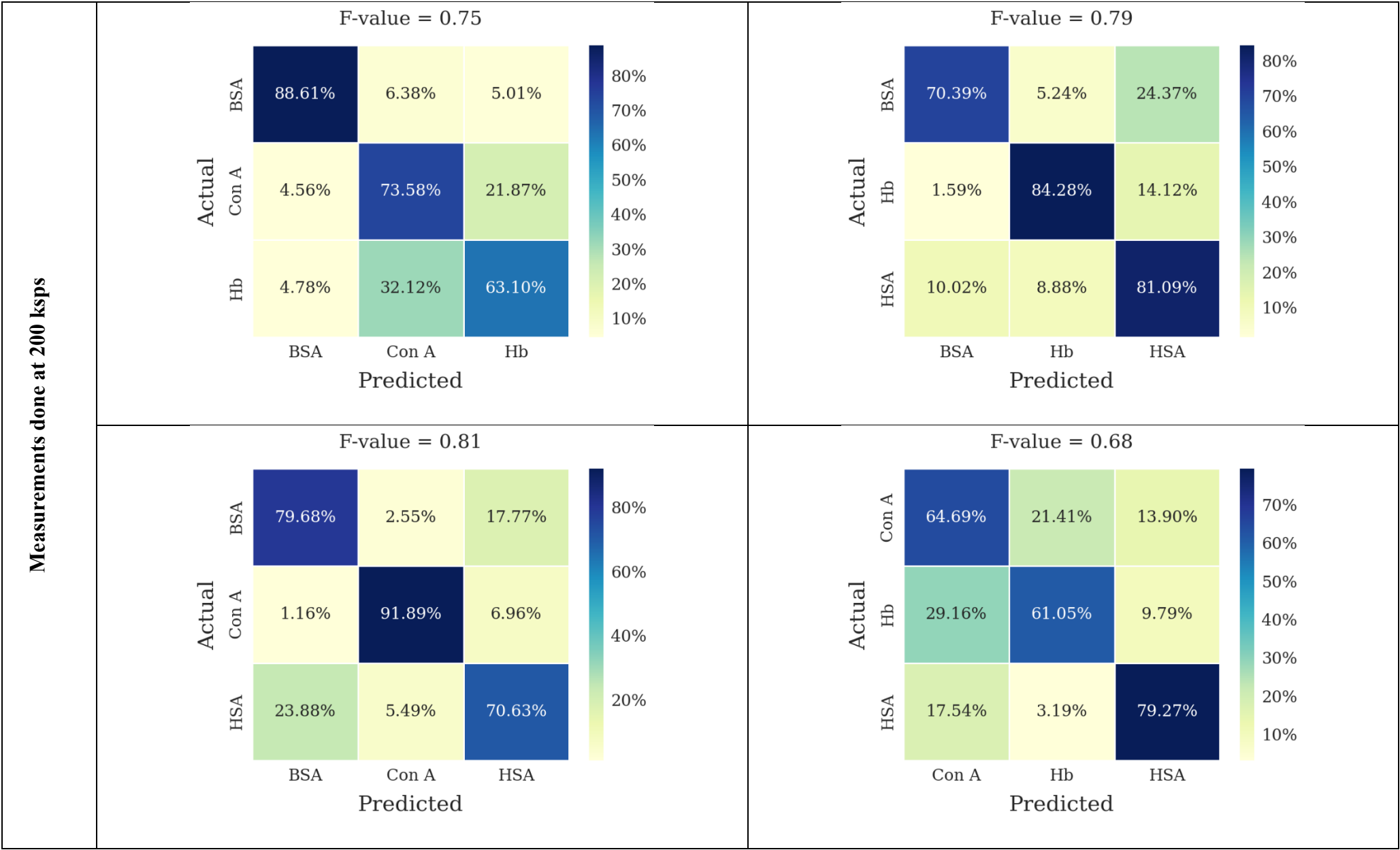
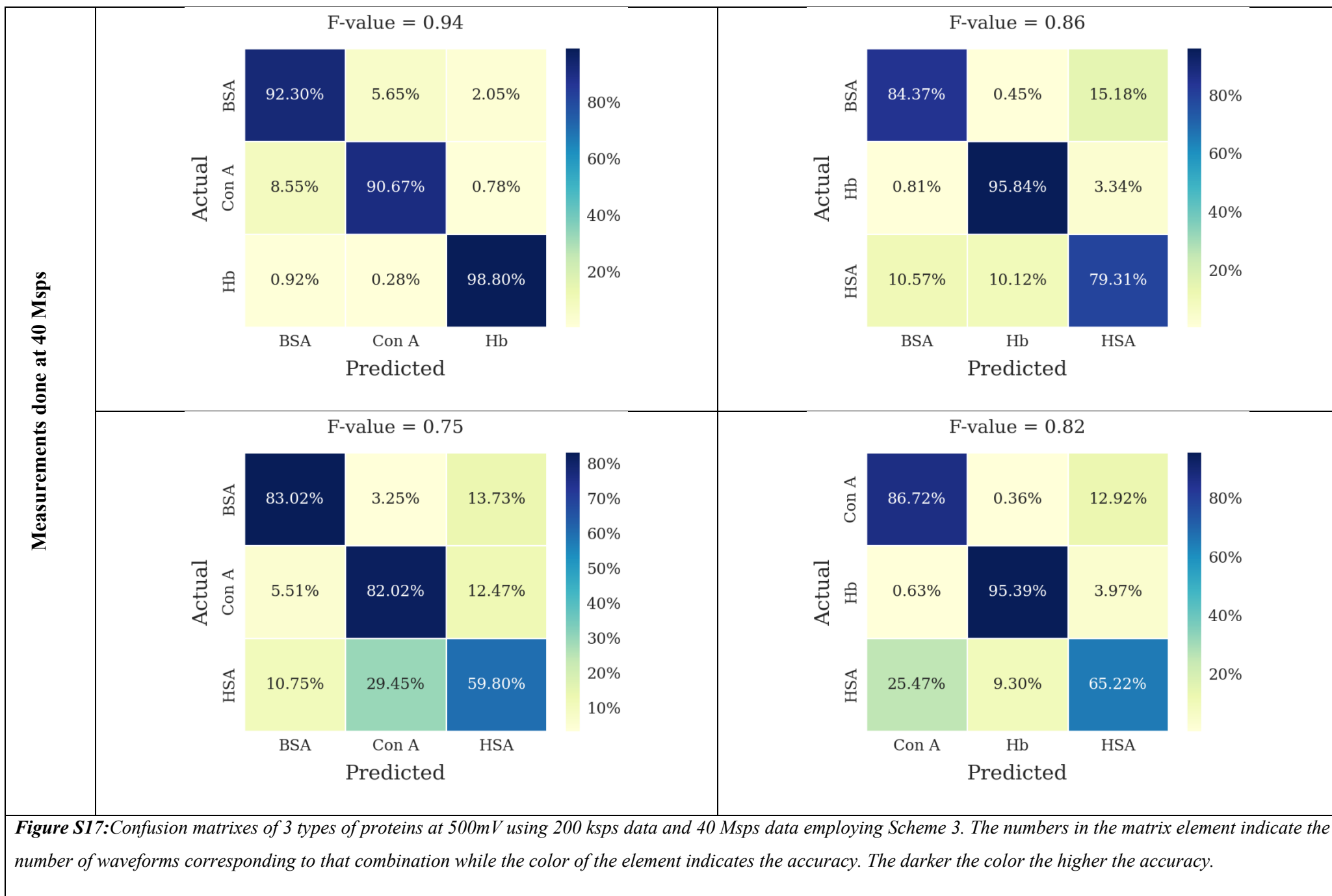


Figure S16: Confusion matrixes of 3 types of proteins at 400mV using 200 kps data and 40 Msps data employing Scheme 3. The numbers in the matrix element indicate the number of waveforms corresponding to that combination while the color of the element indicates the accuracy. The darker the color the higher the accuracy.





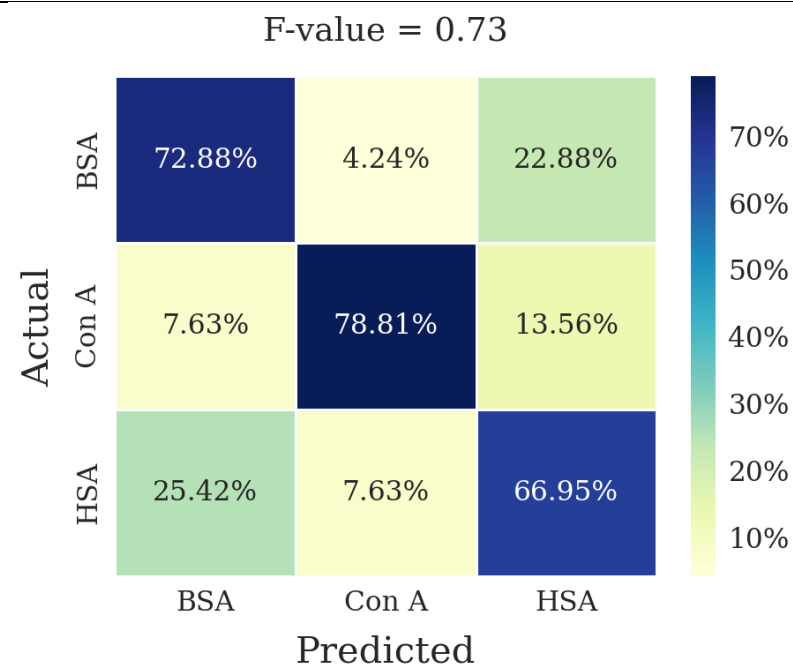


Figure S 18: Confusion matrixes of 3 types of proteins at 600mV using 200 kps data and 40 Mps data employing Scheme 3. The numbers in the matrix element indicate the number of waveforms corresponding to that combination while the color of the element indicates the accuracy. The darker the color the higher the accuracy.

